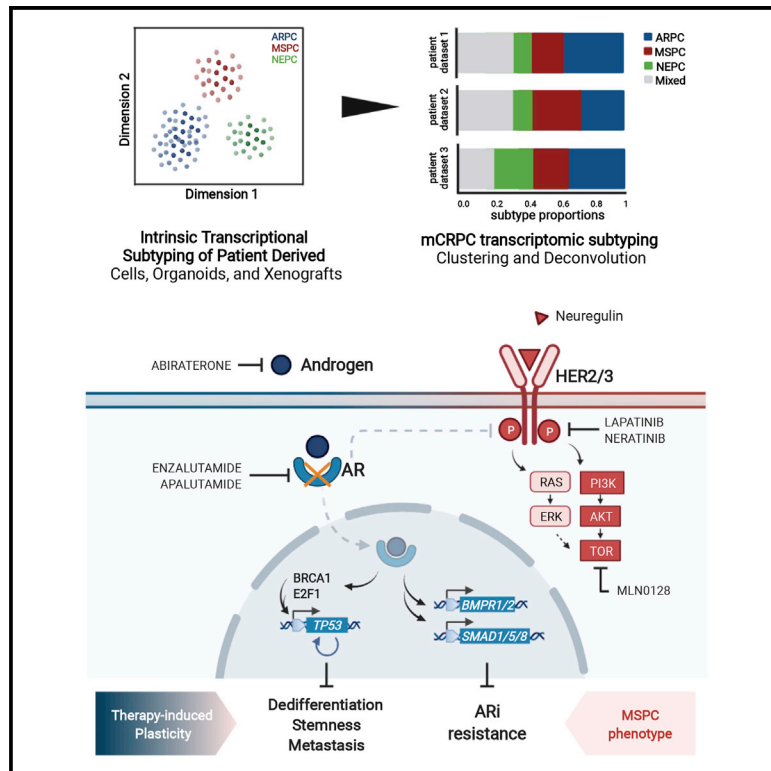# Mesenchymal and stem-like prostate cancer linked to therapy-induced lineage plasticity and metastasis

Graphical abstract

Authors

Hyunho Han, Yan Wang, Josue Curto, ...,
Nora M. Navone, Yu Chen,
Filippo G. Giancotti

Correspondence

fg2532@cumc.columbia.edu

In brief

Han et al. identify mesenchymal stem-like PC (MSPC) as an increasingly sizable subtype of M-CRPC and trace its origin to therapy-induced plasticity. AR blockade induces reprogramming to a stem-like state characterized by hybrid epithelial and mesenchymal (E/M) traits and clinical aggressivity. Drug-persistent MSPC cells are rescued by exogenous NRG1 and generate metastases.

Highlights

- Three intrinsic transcriptional subtypes of prostate cancer are identified

- AR blockade reprograms ARPC cells to HER2/3[+], NRG1-dependent, and metastatic MSPC cells

- Inhibition of TP53 and BMP-SMAD induces reprogramming to MSPC and therapy-resistance

- Neratinib-based combinations are effective in MSPC and mixed ARPC and MSPC xenograft models

CelPress

Cell Reports

Article

Mesenchymal and stem-like prostate cancer linked to therapy-induced lineage plasticity and metastasis

Hyunho Han,[1,3,12] Yan Wang,[1,2,12] Josue Curto,[1,2,13] Sreeharsha Gurrapu,[1,2,13] Sara Laudato,[1,11,13] Alekya Rumandla,[1,4,13] Goutam Chakraborty,[5,9] Xiaobo Wang,[1,2,4] Hong Chen,[1] Yan Jiang,[1] Dhiraj Kumar,[1,2] Emily G. Caggiano,[1,4] Monica Capogiri,[1] Boyu Zhang,[1] Yan Ji,[1] Sankar N. Maity,[6] Min Hu,[7] Shanshan Bai,[7] Ana M. Aparicio,[6] Eleni Efstathiou,[6,10] Christopher J. Logothetis,[6] Nicholas Navin,[7] Nora M. Navone,[6] Yu Chen,[8] and Filippo G. Giancotti[1,2,14,*]

[1]Department of Cancer Biology, UT MDACC, Houston, TX 77054, USA
[2]Herbert Irving Comprehensive Cancer Center and Department of Genetics and Development, Vagelos College of Physicians and Surgeons, Columbia University, New York, NY 10032, USA
[3]Department of Urology, Urological Science Institute, Yonsei University College of Medicine, Seoul 03722, Republic of Korea
[4]UT MDACC UT Health Graduate School of Biomedical Sciences, Houston, TX 77030, USA
[5]Cell Biology Program, MSKCC, New York, NY 10065, USA
[6]Department of GU Oncology, UT MDACC, Houston, TX 77054, USA
[7]Department of Genetics, UT MDACC, Houston, TX 77054, USA
[8]Human Oncology and Pathogenesis Program and Department of Medicine, MSKCC, New York, NY 10065, USA
[9]Present address: Department of Urology and Center of Excellence for Prostate Cancer, Tisch Cancer Institute, Icahn School of Medicine at Mount Sinai, New York, NY 10029, USA
[10]Present address: GU Medical Oncology, Houston Methodist Hospital, Houston, TX 77030, USA
[11]Present address: Tolremo Therapeutics AC, Muttenz, Switzerland
[12]These authors contributed equally
[13]These authors contributed equally
[14]Lead contact
*Correspondence: fg2532@cumc.columbia.edu
https://doi.org/10.1016/j.celrep.2022.110595

SUMMARY

Bioinformatic analysis of 94 patient-derived xenografts (PDXs), cell lines, and organoids (PCOs) identifies three intrinsic transcriptional subtypes of metastatic castration-resistant prostate cancer: androgen receptor (AR) pathway + prostate cancer (PC) (ARPC), mesenchymal and stem-like PC (MSPC), and neuroendocrine PC (NEPC). A sizable proportion of castration-resistant and metastatic stage PC (M-CRPC) cases are admixtures of ARPC and MSPC. Analysis of clinical datasets and mechanistic studies indicates that MSPC arises from ARPC as a consequence of therapy-induced lineage plasticity. AR blockade with enzalutamide induces (1) transcriptional silencing of *TP53* and hence dedifferentiation to a hybrid epithelial and mesenchymal and stem-like state and (2) inhibition of BMP signaling, which promotes resistance to AR inhibition. Enzalutamide-tolerant LNCaP cells re-enter the cell cycle in response to neuregulin and generate metastasis in mice. Combined inhibition of HER2/3 and AR or mTORC1 exhibits efficacy in models of ARPC and MSPC or MSPC, respectively. These results define MSPC, trace its origin to therapy-induced lineage plasticity, and reveal its sensitivity to HER2/3 inhibition.

INTRODUCTION

Dedifferentiation and transdifferentiation play a crucial role in tumorigenesis and metastasis (Boumahdi and de Sauvage, 2020; Gupta et al., 2019). A form of plasticity known as neuroendocrine (NE) transformation promotes resistance to epidermal growth factor receptor (EGFR) inhibitors in lung cancer and androgen receptor (AR) inhibitors in prostate cancer (PC). In these cancers, mutation of *TP53* and *RB1* promotes transdifferentiation and drug resistance by activating alternative survival and proliferation pathways (Quintanal-Villalonga et al., 2020).

BRAF and MEK kinase inhibitors reprogram highly proliferative MITF^high-AXL^low tumor cells into drug-tolerant MITF^low-AXL^high quiescent tumor cells (Arozarena and Wellbrock, 2019). Similarly, adaptive resistance is associated with the acquisition of mesenchymal traits in cancer cell lines exposed to antimitotic therapy (Hangauer et al., 2017). Yet the role of clonal selection and epithelial plasticity in drug resistance and metastasis is still unclear in many cancers.

Prostate adenocarcinoma progresses from a hormone-deprivation-sensitive stage to a castration-resistant and metastatic stage (M-CRPC), which becomes rapidly recalcitrant to therapy.
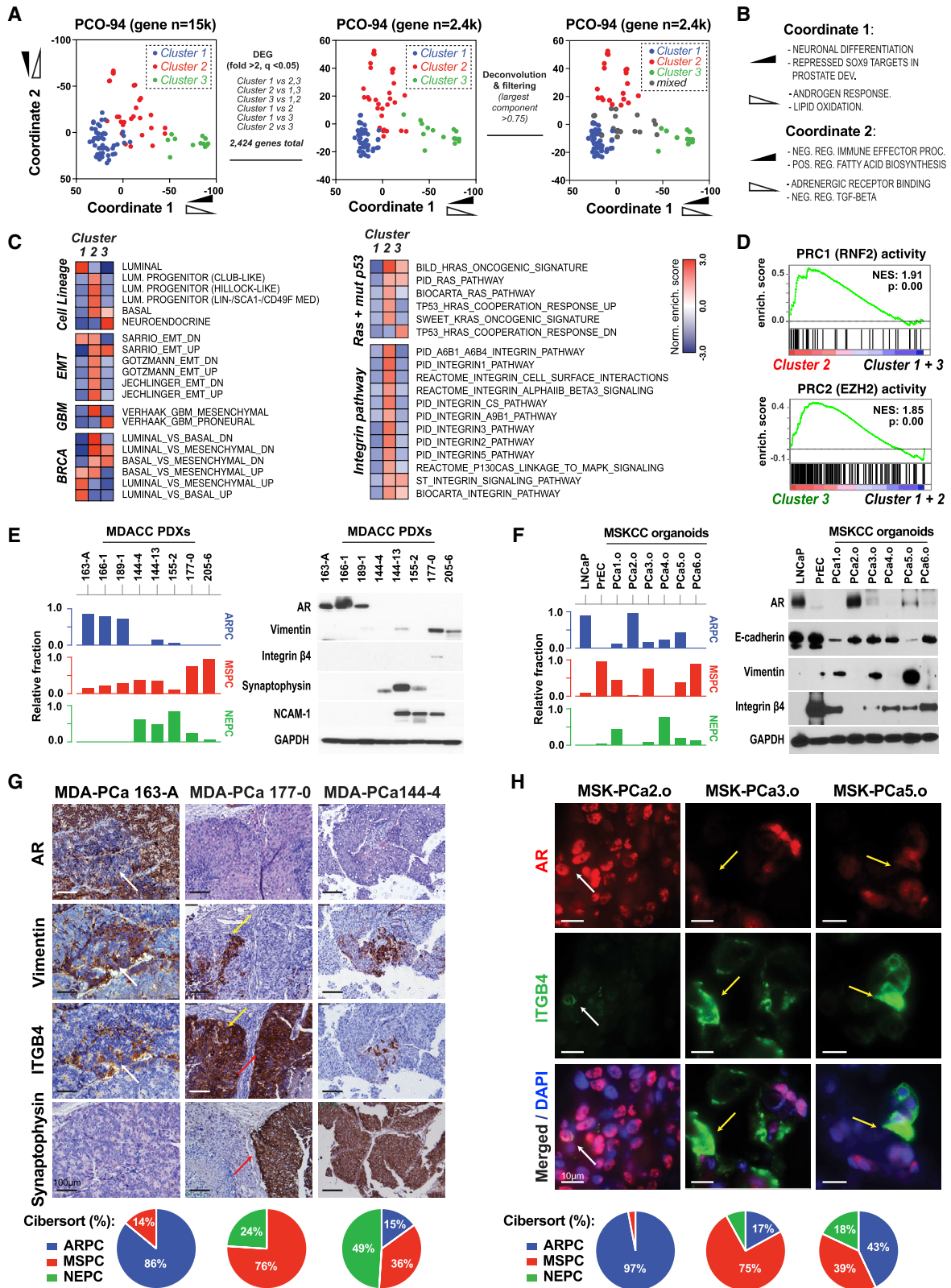
(legend on next page)

Several mechanisms of resistance to AR inhibition have been proposed, including amplification and/or mutation of *AR*, overexpression of the V7 splice variant, co-option of AR signaling by the glucocorticoid receptor, and acquisition of mutations or activation of signaling pathways that alleviate the need for AR signaling (Watson et al., 2015). AR signaling inhibitors (ARSIs), such as enzalutamide and abiraterone, have improved patient survival but have not eradicated the disease (de Bono et al., 2011; Scher et al., 2012). About 30% of patients exhibit primary resistance to these agents and almost all responders eventually develop secondary resistance, highlighting the importance of identifying clinically relevant mechanisms of resistance.

Recent studies have pointed to an AR-independent subtype of M-CRPC devoid of neuroendocrine traits (AR pathway negative, NE negative, or double-negative PC [DNPC]; Bluemn et al., 2017). Yet the origin and nature of this group of cancers remain unclear. It is not known whether these cancers exist at the time of diagnosis or arise from therapy-induced lineage plasticity and whether this reprogramming can occur in the absence of *TP53* and *RB1* mutations. In addition, it is important to determine whether the AR-low PC cells in these cancers rely on alternative pathways that can be targeted therapeutically.

RESULTS

Intrinsic transcriptional subtyping identifies AR pathway + PC, mesenchymal and stem-like PC, and NE PC

To identify transcriptional subtypes of M-CRPC, we initially performed unsupervised clustering of the SU2C-Prostate Cancer Foundation (PCF) dataset (Robinson et al., 2015). Partition around medoids (PAM) identified four clusters, which correlated to a significant extent with the site of origin of metastases (Gardeux et al., 2017; Su et al., 2004; Figure S1A). To eliminate the confounding effect of stromal contamination, we collected the intrinsic transcriptional profiles of a panel of patient-derived xenografts (PDXs), cell lines, and organoids (PCOs) (n = 94; of which 20 newly sequenced) and identified three clusters, which were validated as stable and robust by using consensus clustering and the proportion of ambiguously clustered pairs (PAC) (Figures S1B–S1D). Non-linear methods, such as uniform manifold approximation and projection (UMAP) or t-distributed stochastic neighbor embedding (tSNE),

also identified three clusters (H.H. and F.G.G., unpublished data). Pairwise comparison of the three clusters led to the definition of 2,424 differentially expressed genes (false discovery rate [FDR] < 0.05 and fold change > 2), which retained an intact clustering ability when compared with the whole transcriptome (Figure 1A; Table S1).
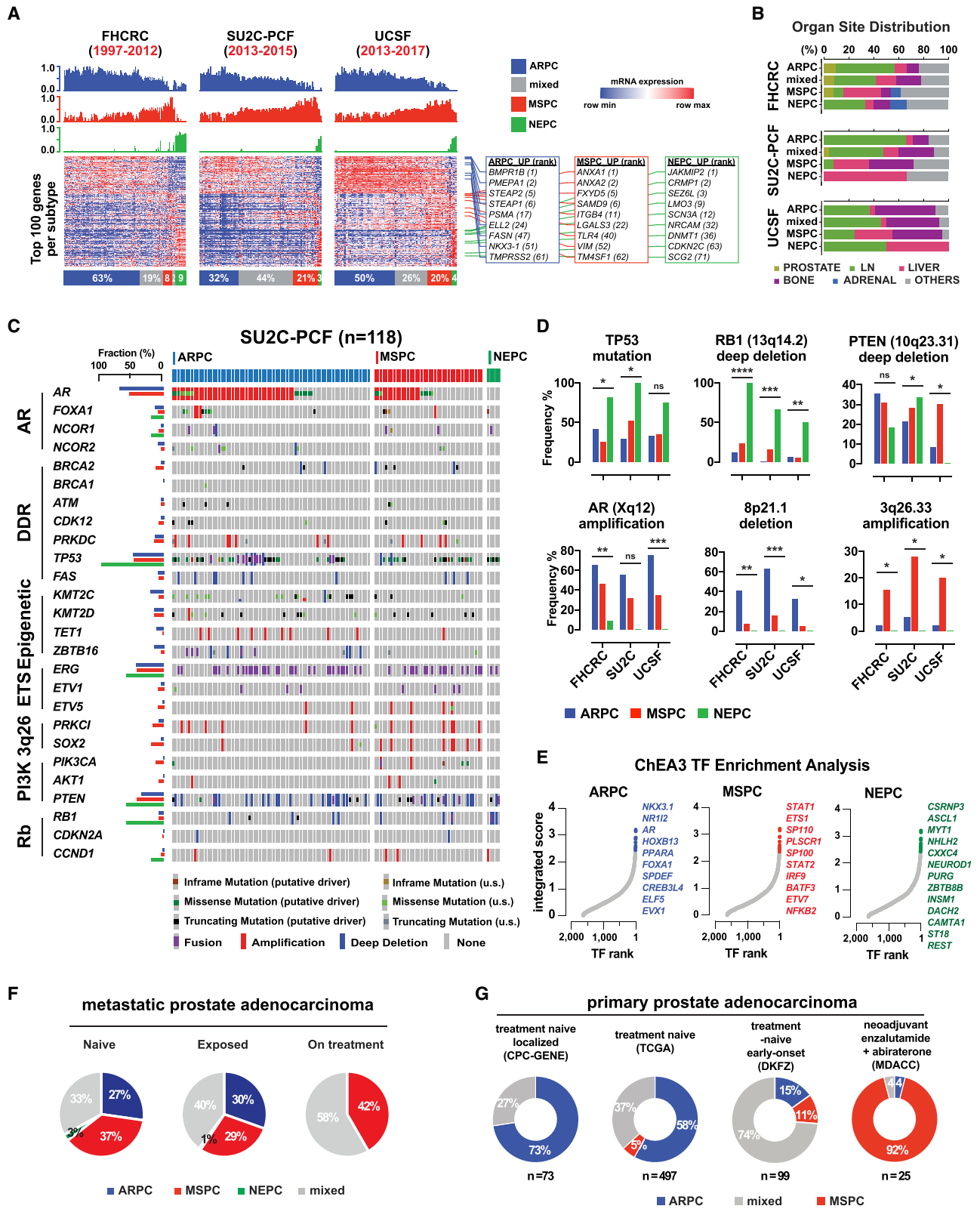
Gene set enrichment analysis (GSEA) revealed that cluster 1 is dominated by the expression of AR target and lipid oxidation genes, cluster 2 by genes involved in the interferon response, tumor necrosis factor alpha (TNF-α) signaling mediated by nuclear factor κB (NF-κB), and transforming growth factor β (TGF-β) signaling, and cluster 3 by genes associated with spermatogenesis and cell cycle (Figures 1B and S1E; Table S2). Consistent with its AR pathway activity, cluster 1 was also enriched of signatures associated with primary prostate luminal cells and luminal breast cancer. In contrast, cluster 3 expressed signatures associated with prostate NE cells and the proneural subtype of glioblastoma multiforme (GBM). Finally, cluster 2 was enriched of signatures associated with prostate luminal progenitors (Henry et al., 2018; Sackmann Sala et al., 2017), the epithelial to mesenchymal transformation (EMT), the mesenchymal subtype of GBM, and basal-like breast cancer (Figure 1C, left). Further analysis indicated that cluster 2 is enriched of genes associated with PC in mouse models (Acevedo et al., 2007; Azare et al., 2007; Liu et al., 2009), RAS and mutant TP53 pathway activation, and integrin signaling (Figures 1C right, S1F, and S1G) (Tomlins et al., 2007; Wallace et al., 2008). In addition, it displayed an enrichment of the PRC1 (RNF2) signature, which we previously linked to both stemness and immune evasion in DNPC (Su et al., 2019). In contrast, cluster 3 was enriched of the PRC2 (EZH2) signature (Figure 1D). Based on their intrinsic programs of gene expression, we defined cluster 1 as AR pathway + PC (ARPC), cluster 2 as mesenchymal and stem-like PC (MSPC), and cluster 3 as NE PC (NEPC).

CIBERSORT reveals intratumoral heterogeneity

To examine whether the PCOs harbor intratumoral heterogeneity, we applied CIBERSORT deconvolution analysis (Newman et al., 2015). Strikingly, we found that about 20% of the PCOs consist of admixtures of two or more transcriptional profiles, even at a purity cutoff of 75% (Figure S2A). In contrast, all eight cell lines showed high purity (>75%; Figure S2B). Examination

---

Figure 1. Intrinsic transcriptomic subtyping and heterogeneity of PCOs

(A) Left: principal coordinate analysis (PCoA) of the total (left), differentially expressed (DE) (middle), and purity annotated (right) PCO-94 transcriptomes. Clustering by PAM is shown. Annotation for purity by deconvolution analysis is shown ("mixed" if largest fraction <75%).

(B) Top gene sets correlated with principal coordinates 1 and 2 of the PCO-94 PCoA. Signatures from the C2 "curated," C5 "Gene Ontology," and H "hallmark" gene sets from the mSigDB collection. Ranking by Pearson correlation "r" of ssGSEA scores and coordinate values is shown. Black triangle, negative correlation; blank triangle, positive correlation.

(C) Normalized enrichment score (NES) heatmap of GSEA of the three clusters. Cell lineage, subsets of human prostate epithelial cells defined by scRNA-seq; EMT, MCF-10A breast cancer (BRCA) cells undergoing EMT (Sarrio et al., 2008). MMH-RT hepatocytes response to TGF-β are shown (Gotzmann et al., 2006). Response of Ras-transformed EpH4 BRCA cells to TGF-β is shown (Jechlinger et al., 2003). GBM, molecular subtypes; BRCA, molecular subtypes (Charafe-Jauffret et al., 2006). Ras + mut p53 and integrin pathway from the MSigDB is shown.

(D) PRC1 signature "genes upregulated by RNF2" and PRC2 signature PRC2_EZH2_UP.V1_UP (M2737) are from the MSigDB (Bracken et al., 2006).

(E and F) Predicted relative fractions (0–1) of ARPC (cluster 1, blue color), MSPC (cluster 2, red), and NEPC (cluster 3, green) in the indicated PDXs (E) and organoids (F; left). Immunoblots (IBs) of PDXs (E) and organoids (F) are shown (right).

(G and H) Immunohistochemistry (IHC) (G) and immunofluorescence (IF) (H) of the indicated PDXs (G) and organoids (H). Representative fields are shown. Scale bars represent 100 μm (G) and 10 μm (H). Pie charts indicate the relative fractions (%) of ARPC, MSPC, and NEPC in each sample. Representative images of n = 3 technical replicates are shown.

A

FHCRC
(1997-2012)

SU2C-PCF
(2013-2015)

UCSF
(2013-2017)

ARPC
mixed
MSPC
NEPC

mRNA expression
row min — row max

Top 100 genes per subtype

63% 19% 8 9
32% 44% 21% 3
50% 26% 20% 4

ARPC_UP (rank)	MSPC_UP (rank)	NEPC_UP (rank)
BMPR1B (1)	ANXA1 (1)	JAKMIP2 (1)
PMEPA1 (2)	ANXA2 (2)	CRMP1 (2)
STEAP2 (5)	FXYD5 (5)	SEZ6L (3)
STEAP1 (6)	SAMD9 (6)	LMO3 (9)
PSMA (17)	ITGB4 (11)	SCN3A (12)
ELL2 (24)	LGALS3 (22)	NRCAM (32)
FASN (47)	TLR4 (40)	DNMT1 (36)
NKX3-1 (51)	VIM (52)	CDKN2C (63)
TMPRSS2 (61)	TM4SF1 (62)	SCG2 (71)

B

Organ Site Distribution

(%) 0 20 40 60 80 100

FHCRC
ARPC
mixed
MSPC
NEPC

SU2C-PCF
ARPC
mixed
MSPC
NEPC

UCSF
ARPC
mixed
MSPC
NEPC

PROSTATE LN LIVER
BONE ADRENAL OTHERS

C

SU2C-PCF (n=118)

Fraction (%) 100 50 0

ARPC MSPC NEPC

AR:
AR
FOXA1
NCOR1
NCOR2

DDR:
BRCA2
BRCA1
ATM
CDK12
PRKDC
TP53
FAS

Epigenetic:
KMT2C
KMT2D
TET1
ZBTB16

ETS:
ERG
ETV1
ETV5

3q26:
PRKCI
SOX2

PI3K:
PIK3CA
AKT1
PTEN

Rb:
RB1
CDKN2A
CCND1

Inframe Mutation (putative driver)   Inframe Mutation (u.s.)
Missense Mutation (putative driver) Missense Mutation (u.s.)
Truncating Mutation (putative driver) Truncating Mutation (u.s.)
Fusion   Amplification   Deep Deletion   None

D

TP53 mutation

Frequency % 100 50 0
* * ns

RB1 (13q14.2) deep deletion
**** *** **

PTEN (10q23.31) deep deletion
40 30 20 10 0
ns * *

AR (Xq12) amplification
Frequency % ** ns ***

8p21.1 deletion
80 60 40 20 0
** *** *

3q26.33 amplification
30 20 10 0
* * *

FHCRC SU2C UCSF

ARPC MSPC NEPC

E

ChEA3 TF Enrichment Analysis

ARPC
integrated score
4 3 2 1 0
NKX3.1
NR1I2
AR
HOXB13
PPARA
FOXA1
SPDEF
CREB3L4
ELF5
EVX1
2,000 1,000 1
TF rank

MSPC
STAT1
ETS1
SP110
PLSCR1
SP100
STAT2
IRF9
BATF3
ETV7
NFKB2
2,000 1,000 1
TF rank

NEPC
CSRNP3
ASCL1
MYT1
NHLH2
CXXC4
NEUROD1
PURG
ZBTB8B
INSM1
DACH2
CAMTA1
ST18
REST
2,000 1,000 1
TF rank

F

metastatic prostate adenocarcinoma

Naive
33% 27%
3% 37%

Exposed
40% 30%
1% 29%

On treatment
58% 42%

ARPC MSPC NEPC mixed

G

primary prostate adenocarcinoma

treatment naive localized (CPC-GENE)
27% 73%
n=73

treatment naive (TCGA)
37% 58% 5%
n=497

treatment-naive early-onset (DKFZ)
15% 11% 74%
n=99

neoadjuvant enzalutamide + abiraterone (MDACC)
4 4 92%
n=25

ARPC mixed MSPC

(legend on next page)

of the LuCaP PDXs and organoids (Nguyen et al., 2017) confirmed the results obtained with the PCOs (Figure S2C). Early- and late-passage organoids and PDXs maintained a similar transcriptional composition, and organoid-derived xenografts (ODXs) were similar to the tumor organoids from which they were generated, suggesting that propagation *in vitro* or *in vivo* does not favor the emergence and dominance of a specific transcriptional state (Figure S2D). Similar conclusions were reached independently of whether the transcriptional profiles were obtained from DNA microarray or RNA sequencing (Figure S2E).

To validate these findings, we examined the expression of AR and luminal differentiation markers, mesenchymal and stem cell markers, and NE markers in a subset of UT MD Anderson Cancer Center (MDACC) PDXs and Memorial Sloan Kettering Cancer Center (MSKCC) organoids (Figures 1E and 1F, left). Immunoblotting indicated that samples containing a large ARPC component express AR and those enriched of an NEPC component synaptophysin. Samples with predominant MSPC component exhibit instead robust expression of the mesenchymal marker vimentin and/or the prostate stem cell marker ITGB4 (Yoshioka et al., 2013; Figures 1E and 1F, right). Consistent with the intratumoral heterogeneity predicted from deconvolution analysis, immunohistochemical staining of PDXs indicated that the mesenchymal and stem cell or the NE markers were restricted to subpopulations of tumor cells (Figure 1G). In addition, immunofluorescent staining of ARPC, MSPC, and mixed ARPC-MSPC organoids revealed a mutually exclusive expression of AR and ITGB4 (Figure 1H). We therefore concluded that the PCOs consist of different proportions of tumor cells expressing the ARPC, MSPC, or NEPC transcriptional program.

Transcriptomic, immunologic, and genetic characteristics of ARPC, MSPC, and NEPC in patients

To examine the characteristics of ARPC, MSPC, and NEPC in patients, we used the 2,424 genes differentially expressed by the three PCO subtypes to perform clustering and deconvolution of the M-CRPC samples from the SU2C-PCF (Robinson et al., 2015), Fred Hutchinson Cancer Research Center (FHCRC) (Kumar et al., 2016), and University of California, San Francisco (UCSF) datasets (Quigley et al., 2018). This analysis identified in each dataset three clusters indistinguishable from the PCO subtypes ARPC, MSPC, and NEPC (Figure S3A). After filtering out mixed samples by deconvolution (<60% pure), we generated subtype-specific gene expression heatmaps (Figure 2A; Table S3). We noted that ARPC cases overexpress the BMP receptor

BMPR1B and the prostate-specific membrane antigen FOLH1, a target of the Lu-177-labeled therapeutic antibody (Sartor et al., 2021). In contrast, MSPCs overexpressed annexin A1 (*ANXA1*), a diagnostic marker in hairy cell leukemia (Falini et al., 2004), and TM4SF1, which mediates metastatic reactivation in breast cancer (Gao et al., 2016). In addition, MSPCs overexpressed ITGB4, the EMT regulators ZEB1 and SNAI2, and several canonical EMT genes. Finally, NEPCs exhibited elevated levels of canonical NE marker genes and the Golgi-associated protein JAKMIP2, which controls neuronal secretory function (Cruz-Garcia et al., 2012; Figures 2A and S3B; Table S3).

We next examined the relationship between our classification and the molecular marker-derived (AR/PSA and SYP/CHGA) transcriptional classification (Bluemn et al., 2017). As anticipated, we found that ARPC overlaps with the AR^+NE^- subtype, MSPC with the AR^-NE^- (DNPC), and NEPC with the AR^-NE^+ subtype (Figure S3C). However, MSPC samples included DNPC and a sizable fraction of metastases previously classified as AR^+NE^- or AR^-NE^+. Parenthetically, the extent of overlap between MSPC and DNPC is similar to that observed between the basal-like intrinsic subtype of breast cancer and triple-negative breast cancer (75%–80%; Foulkes et al., 2010).

Evaluation of the proportion of distant metastatic sites consisting predominantly of one subtype revealed that MSPC is present in both bone and liver metastases across datasets. As anticipated, ARPC was enriched in bone and NEPC in liver metastases. Adrenal metastases were present only in the FHCRC dataset and tended to track with liver metastases in both MSPC and NEPC (Figure 2B). With the caveat that only one or two metastatic sites were sampled in the majority of patients, these results suggest that MSPC colonizes both the bone and visceral organs.

Consistent with the prominent activation of PRC1 and enrichment of inflammatory signatures in MSPC (Figures 1D and S1F), CIBERSORT revealed an enrichment of myeloid cells, including M2 macrophages, in MSPC cases across the three datasets (Figure S3D). In spite of their enrichment and elevated intratumoral interferon-gamma (IFNγ) activity, tumor immune dysfunction and exclusion (TIDE) scoring (Jiang et al., 2018) suggested that the $CD8^+$ T cells present in MSPC are highly dysfunctional (Figure S3E). Furthermore, we found that MSPC is enriched of the anti-PD-1 nonresponder signature (Hugo et al., 2016; Figure S3F). In contrast, NEPCs were enriched of myeloid derived suppressor cells, which have been implicated in T cell exclusion and YAP-dependent PC progression (Wang et al., 2016; Figure S3D;

Figure 2. Biological and clinical characteristics of M-CRPC subtypes

(A) Relative fraction of ARPC, MSPC, and NEPC in the indicated M-CRPC datasets. Years of collection are in brackets. Sample data aligned following the order of the heatmap (top) are shown. Heatmap of the top 100 genes upregulated in each subtype is shown. Columns are grouped by subtype and sorted by hierarchical clustering (bottom). Selected upregulated genes in each subtype are shown. Their mRNA expression rank was calculated by using the lowest max false discovery rate (FDR max) for each dataset and is shown in brackets (right).

(B) Organ site distribution of the M-CRPC samples by subtype.

(C) Common genetic alterations of ARPC, MSPC, and NEPC in the SU2C-PCF dataset. Oncoprint was generated in cBioPortal.org (Cerami et al., 2012). DDR, DNA damage repair; u.s., unknown significance.

(D) Signature genetic alterations in ARPC, MSPC, and NEPC in the three datasets. p value was calculated by chi-square test. ns, not significant; *p < 0.05; **p < 0.01; ***p < 0.001; ****p < 0.0001.

(E) ChEA3 TF enrichment analysis of the promoters of the genes upregulated in ARPC, MSPC, and NEPC.

(F) Deconvolution analysis of the SU2C-PCF dataset. Samples are stratified by ARSI exposure status.

(G) Deconvolution analysis of the CPC-GENE dataset, the TCGA dataset, the DKFZ dataset, and the MDACC dataset.

Table S4). These results suggest that MSPC and NEPC comprise distinct immune-suppressive tumor microenvironments.

In agreement with their role as initiating events, *PTEN* deletions and mutations and *ERG* fusions were common in all three transcriptional subtypes. Notably, ARPC and MSPC harbored a similar repertoire of cancer gene mutations, including *AR* amplifications and mutations (Figures 2C and 2D). However, whereas the deletion of chromosome (Chr) 8p21.1 was specifically enriched in ARPC, the amplification of Chr 3q26.33 was moderately enriched in MSPC metastases (10%–20% across datasets), organoids, and cell lines (Figures 2C, 2D, and S3G). Chr 8p21.1 contains multiple genes involved in lipid metabolism and sensitivity to anti-cancer drugs (Cai et al., 2016; Xue et al., 2012), and 3q26.33 comprises three oncogenes, *SOX2*, *FXR1*, and *PRKCI* (Bass et al., 2009; Justilien et al., 2014; Qian et al., 2015). These findings indicate that ARPC and MSPC harbor similar oncogenic alterations with the possible exception of distinctive allelic imbalances at 8p21.1 and 3q26.33.

As anticipated, *RB1* deletions and *TP53* mutations were considerably enriched in NEPC (Figures 2C and 2D). Analysis of a dataset comprising CRPC-adeno and CRPC-NE (Beltran et al., 2016) showed that the NEPC component is specifically enriched in *RB1*-mutated or deleted CRPC samples (Figure S4A). A reanalysis of the MDACC PDXs (Navone et al., 2018) confirmed that the NE histology and the complete loss of *RB1* were exclusive to the transcriptionally defined NEPC PDXs (Figure S4B). In addition, the NEPC metastases were enriched of the loss of *RB1* signature (Figure S4C). Together, these results support the hypothesis that NEPC arises as a result of clonal selection following loss of *TP53* and *RB1*.

To identify the top transcription factors (TFs) controlling the ARPC, MSPC, and NEPC transcriptomes, we used ChEA3 TF enrichment analysis (Keenan et al., 2019). Notably, we found that the STAT1/2, ETS1, and NFKB1/2 cistromes dominate the transcriptional program of MSPC (Figure 2E; Table S5). As anticipated, the NKX3.1, AR, FOXA1, and HOXB13 cistromes were prevalent in ARPC and the ASCL1, NEUROD1, and REST cistromes in NEPC (Kron et al., 2017; Labrecque et al., 2019; Park et al., 2018; Pomerantz et al., 2015, 2020). Finally, analysis of the RNAi screening data from the cancer dependency map (Boehm et al., 2021) indicated that the MSPC cell lines are highly dependent on *TEAD1* and *PAX7* and the ARPC lines on *MED12* and *BIRC5*. Lastly, the only NEPC cell line examined was dependent on *SOX2* and *KLF4*, consistent with earlier studies (Mu et al., 2017; Figure S3H; Table S5). Therefore, despite their genetic similarity, ARPC and MSPC possess distinct transcriptional drivers, gene expression programs, and dependencies.

MSPC is associated with acute AR pathway inhibition and poor prognosis

The proportion of mixed ARPC and MSPC and MSPC among subtypes of M-CRPC increased from 19% and 8% in the oldest dataset (FHCRC) to 26% and 20% in the most recent dataset (UCSF), suggesting that exposure to ARSIs contributes to the emergence of MSPC (Figure 2A). To further examine this hypothesis, we stratified the samples from the newer SU2C-PCF M-CRPC dataset (Abida et al., 2019) according to drug-exposure status. Intriguingly, the proportion of MSPC was significantly higher, and the propor-

tion of ARPC significantly lower, in samples on treatment as compared with the remainder. The proportion of NEPC was very low across status groups (Figures 2F and S5A). Neither the AR score nor the NEPC score defined by Abida and colleagues (Abida et al., 2019) was able to stratify the samples according to exposure status (Figure S5B). Furthermore, the patients with MSPC (proportion >60%) who had been treated with ARSIs exhibited poorer overall survival as compared with those with other subtypes who underwent similar treatment (Figure S5C). Collectively, these findings suggest that exposure to ARSIs contributes to the emergence of MSPC.
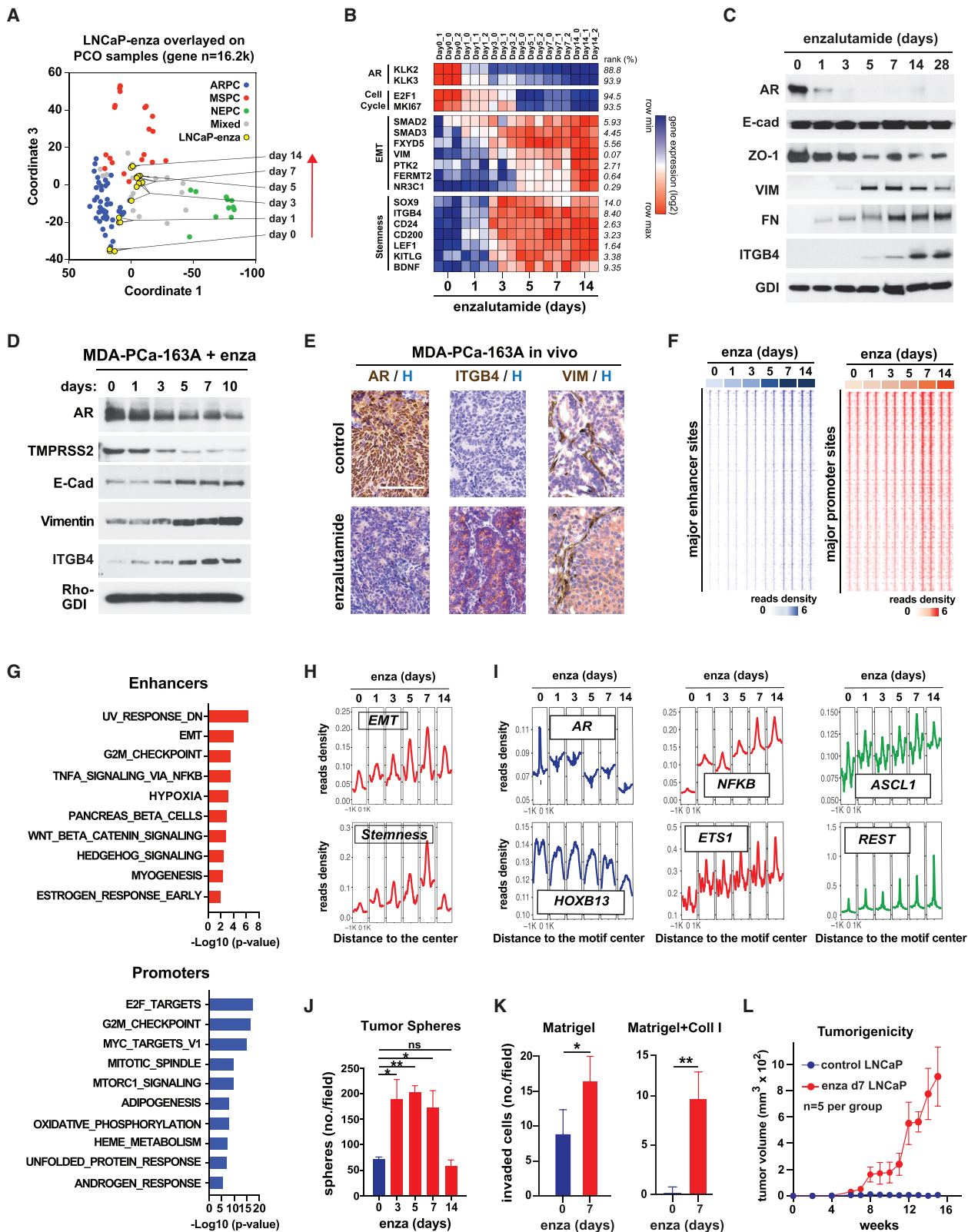
Primary MSPC can arise *de novo* or in response to ARSIs

To examine whether MSPC can originate at the primary site *de novo* or following treatment with ARSIs, we examined the The Cancer Genome Atlas (TCGA) dataset, which consists of treatment-naive PCs of all T stages, Gleason scores, and patient ages; the Canadian Prostate Cancer Genome Network (CPC-GENE) dataset, which includes treatment-naive localized non-indolent PCs (Gleason score 6–7; Fraser et al., 2017); the Deutsches Krebsforschungszentrum (DKFZ) dataset, which comprises early-onset, treatment-naive PCs (patient age <55; Gerhauser et al., 2018); and the MDACC dataset, consisting of locally advanced high-risk PCs, which received neoadjuvant abiraterone and/or enzalutamide for 24 weeks without undergoing significant shrinkage (MDACC dataset, Gleason score ≥8 or clinical stage ≥T2b; Efstathiou et al., 2016). Primary tumor samples were classified as ARPC (ARPC component >60%), MSPC (MSPC component >60%), or mixed. Intriguingly, we found that the MSPC component is enriched modestly in the TCGA dataset (5%) and to a higher extent (11%) in the treatment-naïve, early-onset DKFZ dataset in comparison with the CPC-GENE dataset (Figure 2G). Notably, MSPC samples were enriched of *TP53* mutations (31%–54%) and *PTEN* deletions (39%; Figure S5D). In addition, they were more advanced than primary ARPC or mixed samples in terms of Gleason score, pathologic T stage, and N stage (Figures S5E and S5F). Finally, a higher proportion of patients with primary MSPC exhibited accelerated progression and succumbed to the disease within 24 months of diagnosis (Figures S5G–S5I). These findings indicate that *de novo* MSPC is associated with accelerated progression.

To directly examine the effect of therapy on primary ARPC, we examined the MDACC dataset, which comprises primary cancers that resisted treatment with ARSIs (Efstathiou et al., 2016). Notably, these tumors exhibited a dramatic enrichment of the MSPC component as compared with historical controls, suggesting that exposure to ARSIs promotes the emergence of MSPC from ARPC (Figures 2G and S5J). Consistent with the rarity of *RB1* loss (1 of 44 samples), the samples did not exhibit any enrichment of the NEPC component. Together, these findings indicate that MSPC can arise at the primary site, either *de novo* or in response to therapy.

Enzalutamide induces dedifferentiation to a therapy-resistant hybrid epithelial and mesenchymal and stem cell state

To model these events *in vitro*, we treated the hormone-responsive *PTEN* mutant LNCaP cells with 10 μM enzalutamide and conducted functional analyses over a 2-week period. Although the drug

A LNCaP-enza overlayed on PCO samples (gene n=16.2k)

B

C enzalutamide (days)

D MDA-PCa-163A + enza

E MDA-PCa-163A in vivo

F enza (days)

G Enhancers / Promoters

H enza (days)

I enza (days)

J Tumor Spheres

K Matrigel / Matrigel+Coll I

L Tumorigenicity

(legend on next page)

inhibited cell growth and provoked apoptosis of an increasing proportion of LNCaP cells at each of the time points, about 20% of the cells survived 14 days of drug treatment and remained viable over additional 2 weeks (Figure S6A). Pulses of bromodeoxyuridine (BrdU) incorporation and staining at 3 and 7 days indicated that the large majority (>95%) of LNCaP cells exposed to enzalutamide undergo cell-cycle arrest in 7 days (Figure S6B). Moreover, inspection of the cultures pulsed with BrDU at day 7 did not reveal any cluster, however small, of positive cells, excluding the possibility that the drug-tolerant cells had arisen from the expansion of rare pre-existing drug-resistant cells. RNA sequencing (RNA-seq) followed by principal coordinate analysis (PCoA) and GSEA confirmed that LNCaP cells exposed to enzalutamide downregulate mitogenic signaling and exit the cell cycle (Figure S6C). These results indicate that a fraction of LNCaP cells treated with enzalutamide become drug tolerant.

Strikingly, superimposition of the time series of transcriptomic profiles of persister LNCaP cells onto the PCoA plot of ARPC, MSPC, and NEPC PCOs revealed that the LNCaP cells change their transcriptional program from ARPC to MSPC over 2 weeks of treatment (Figure 3A). Enzalutamide downregulated AR and mitogenic signaling in 3–5 days and induced EMT and stemness genes with a similar kinetics (Figure 3B). Immunoblotting indicated that the drug-treated LNCaP cells exhibit diminished levels of the AR. Earlier studies had attributed this decrease to diminished mRNA expression and protein stability (Kuruma et al., 2013; Tran et al., 2009). In addition, the LNCaP cells treated with enzalutamide maintained high levels of E-cadherin, but not ZO-1, and acquired expression of vimentin, fibronectin, and ITGB4, which has been linked to the hybrid epithelial and mesenchymal (E/M) state associated with stemness in breast cancer (Bierie et al., 2017; Figure 3C). To examine the generality of these findings, we treated with enzalutamide two additional ARPC models, the VCaP cells and the MDA PCa-163-A PDX, the latter of which was established from a treatment-naive patient (Aparicio et al., 2016; Figures 1E, 1G, and S2B). In agreement with their high sensitivity to the drug (Tran et al., 2009), the majority of VCaP cells underwent cell death within 5 days of treatment with 0.2 μM enzalutamide. However, the cells persisting throughout drug exposure acquired hybrid E/M and stemness traits (Figures S6D and S6E). PC cells explanted from the MDA PCa-163-A PDX underwent a similar phenotypic conversion in response to enzalutamide *in vitro* or upon reimplantation in mice (Figures 3D and 3E). These

observations indicate that hormone-dependent PC cells become tolerant to enzalutamide by acquiring hybrid E/M and stem-like traits and switching their fate from ARPC to MSPC.

To examine the changes in chromatin accessibility underlying the change in cell state induced by enzalutamide, we performed assay for transposase-accessible chromatin using sequencing (ATAC-seq). Annotation of the major peaks indicated that LNCaP cells treated with the drug exhibit a progressive opening of the chromatin at major enhancers and promoters (Figures 3F and S6F–S6H). GSEA revealed that the most affected hallmark 50 signatures are linked to stem cell activity, cell signaling, cell fate, cell cycle, the androgen response, and other functions (Figure 3G). Notably, the chromatin accessibility at the enhancers and promoters of EMT and stemness genes increased substantially during exposure to the drug (Figure 3H). TF binding analysis indicated that enzalutamide decreases the chromatin accessibility of the DNA-binding motifs of the ARPC-specific TFs AR, FOXA1, and HOXB1 and it increases that of MSPC-specific TFs NF-κB and ETS1 (Figure 3I). However, the drug also increased the accessibility of the DNA-binding motifs of NEPC-specific TFs ASCL1 and REST, which do not contribute to the MSPC transcriptional program.

Chromatin immunoprecipitation (ChIP)-seq indicated that enzalutamide decreases the deposition of the repressive histone mark H3K27me3 and increases the deposition of the activation mark H3K4me3 on the promoters of MSPC marker genes. In contrast, it induced reciprocal changes in the deposition of the two marks on the promoters of ARPC marker genes (Figure S6I). Consistently, the deposition of the repressive mark H3K27me3 decreased, and that of the activation mark H3K4me3 increased, at promoters of prototypical mesenchymal and stemness genes (Figure S3J). RNA-seq confirmed a positive enrichment of EMT and stemness gene sets and a negative enrichment of AR targets and cell cycle genes (Figure S6K). Parenthetically, the promoters of NEPC marker genes gradually lost H3K27me3 during enzalutamide treatment but did not acquire higher levels of H3K4me3, suggesting that they had not become active. Therefore, AR blockade induces coordinated and dynamic changes in chromatin accessibility and transcriptional activity, culminating in the downregulation of the AR-driven cistrome, the upregulation of a transcriptional program dominated by ETS1 and NFkB1/2, and the acquisition of hybrid E/M and stem-like traits.

In spite of their quiescence in culture, the enzalutamide-treated cells exhibited a robust increase in tumorsphere formation. This

Figure 3. Exposure to enzalutamide induces E/M and stemness traits and confers tumor initiation capacity

(A) PCoA of the RNA-seq data from the LNCaP enzalutamide time series merged with the PCO-94 dataset. Three replicates per time point are shown.

(B) Gene expression heatmap of AR target, cell cycle, EMT, and stemness genes at the indicated time points in LNCaP cells treated with 1 μM enzalutamide. Rank (%) by using the Pearson correlation coefficient with drug incubation time points (0–14 days) is shown.

(C) IB of AR and EMT of the indicated proteins in the LNCaP enzalutamide time series. Representative blots are shown; n = 3 technical replicates.

(D and E) MDA-PCa-163A cells were treated with 1 μM enzalutamide for the indicated times and subjected to IB. Representative blots of n = 3 technical replicates (D) are shown. At 4 weeks after subcutaneous (s.c.) implantation of MDA-PCa-163A cells, NSG mice were treated with 10 mg/kg/day enzalutamide for 2 weeks. Representative IHC images of the indicated proteins in control and enzalutamide-treated tumors are shown. Scale bar represents 100 μm; n = 5 mice/group. H, hematoxylin (E).

(F–I) ATAC-seq of LNCaP cells at different time points of enzalutamide treatment. Heatmap of ATAC peaks in the −1 to +1 kb around "major" enhancer sites (left) and major promoter sites (right) is shown (F). Hallmark GSEA for major enhancer sites and promoter regions is shown (G). Profile of the promoters of EMT and stemness genes (H) and the motif binding sites for each of the indicated TFs (I) are shown.

(J–L) Spheres per 3,000 LNCaP cells treated with enzalutamide for the indicated times (J). Invasion assay with Matrigel or Matrigel + collagen I (K) is shown. Mean ± SD of triplicate experiments; p value by one-way ANOVA and multiple comparison by Dunnett's test in (J) and two-tailed Student's t test in (K). *p < 0.05; **p < 0.01. Control and enzalutamide-treated LNCaP cells were implanted s.c. in castrated mice. Tumor growth was monitored for 16 weeks. n = 5 mice per group (L).
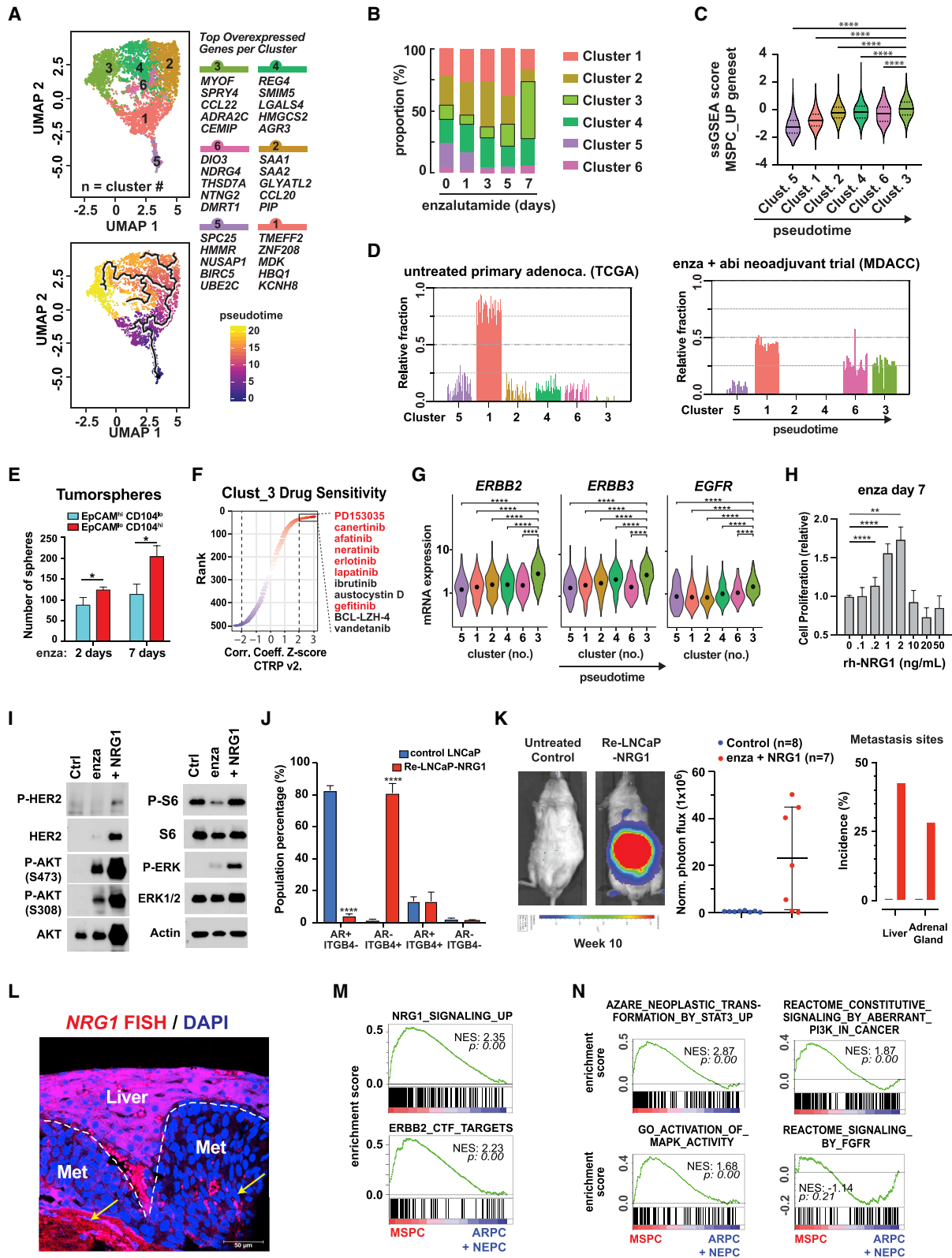
effect decreased during the 2nd week of treatment, possibly due to consolidation of proliferative quiescence (Figure 3J). In addition, they invaded through Matrigel and Matrigel + collagen I *in vitro* to a larger extent than untreated cells (Figure 3K). Finally, whereas the parental controls were not tumorigenic castrated mice, the LNCaP cells treated with enzalutamide for 1 week were able to produce subcutaneous tumors after 1 month of latency (Figure 3L). Thus, although the drug-tolerant LNCaP cells are slowly cycling or quiescent *in vitro*, they manifest oncogenic traits associated with PC stem cells, including high self-renewal capacity *in vitro* and castration-resistant growth *in vivo*.

Single-cell analysis delineates the trajectory from ARPC to MSPC

To further examine the nature of the phenotypic and functional transformation induced by enzalutamide, we performed single-cell RNA-seq (scRNA-seq) of LNCaP cells at various time points of drug exposure. Graph-based clustering defined six closely related cell clusters (Figures 4A, top, and S7A). Although both cluster 5 and 1 cells, which are adjacent in high dimensional space, exhibited AR signaling and MYC activity, only cluster 5 cells expressed G2/M phase genes. In contrast, cluster 2, 4, and 6 cells showed quiescent, mesenchymal, and inflammatory traits. Finally, cluster 3 cells displayed hybrid E/M and stem cell traits and expressed G0/1 phase genes (Figure S7B). Pseudotime analysis suggested that the cells exposed to enzalutamide transit from cluster 5 through cluster 1 and 2 to cluster 4 and that cluster 4 finally morphs into cluster 3 and to a lower extent into cluster 6 (Figures 4A, bottom, and S7B). Consistent with the pseudotime trajectory, analysis of individual time points indicated that cluster 5 cells, which are characterized by the expression of G2/M genes, disappear following enzalutamide treatment. In contrast, cluster 3 cells with hybrid E/M and stem cell traits became the predominant cluster over 7 days of treatment (Figure 4B).

The changes in gene expression occurring during the pseudotime trajectory largely recapitulated the gradual shift from luminal adenocarcinoma to MSPC deduced from bulk RNA-seq data. Congruently, single-sample GSEA indicated that cluster 3 cells

are enriched of signatures associated with the MSPC state, stemness, EMT, and inflammatory signaling and depleted of signatures associated with cell cycle progression (Figures 4C and S7C). Furthermore, cluster 3 cells were enriched of genes overexpressed during embryonic diapause-like dormancy and associated with MYC inactivation and tumor cell persistence against treatment (Boroviak et al., 2015; Dhimolea et al., 2021; Scognamiglio et al., 2016; Figure S7D). Re-examination of the transcriptional profiles of the nonresponders in the MDACC neoadjuvant enzalutamide + abiraterone dataset indicated that the representation of the gene expression programs of clusters 5 and 1 decreased and that of clusters 4 and 2 disappeared in the resistant tumors as compared with untreated reference tumors. Conversely, the representation of the gene expression programs of cluster 3 and, to a somewhat lower degree, cluster 6 increased in persistent tumors (Figure 4D). Collectively, the gene-expression programs associated with cluster 3 and 6 were expressed by 50% of the tumor cells in these tumors, suggesting that a fraction of primary PC cells acquire the gene-expression program associated with cluster 3 and 6 in response to enzalutamide.

Consistent with the observation that cluster 3 cells exhibit the lowest expression of EpCAM and the highest expression of ITGB4 as compared with other clusters (Figure S7E), fluorescence-activated cell sorting (FACS) analysis indicated that the EpCAM^HIGH ITGB4^LOW cells are gradually depleted as the EpCAM^LOW ITGB4^HIGH cells emerge and become predominant during drug treatment (Figure S7F). Notably, EpCAM^LOW ITGB4^HIGH cells isolated by FACS at either day 2 or day 7 formed a higher number of tumorspheres as compared with EpCAM^HIGH ITGB4^LOW cells, functionally validating the association of cluster 3 with stemness (Figure 4E). We concluded that profound inhibition of AR signaling reprograms PC cells to a hybrid E/M and stemness fate in PC cells *in vitro* and in patients' tumors *in vivo*.

Enzalutamide-persistent cells are primed to re-enter the cell cycle in response to exogenous NRG1

Examination of the Cancer Therapeutics Response Portal v.2 (Rees et al., 2016) predicted a specific sensitivity of cluster 3

Figure 4. NRG1 rescues reprogrammed LNCaP cells from quiescence and enables metastasis

(A–D) LNCaP cells were treated with enzalutamide for 0, 1, 3, 5, and 7 days and subjected to scRNA-seq. UMAP plots of LNCaP enzalutamide time series (merged time points) are shown. Clusters were identified by graph-based clustering. Two clusters of low unique molecular identifier (UMI) (gray) were excluded from further analysis (top). Pseudo time analysis and cell fate trajectory by Monocle 3 (bottom) is shown (A). Proportion of clusters at each time point is shown (B). ssGSEA score of MSPC_UP genes in each cluster is shown. p values by one-way ANOVA with multiple comparison by Dunnett's test are shown; ****p < 0.0001 (C). The relative fraction of each cluster in untreated and ARSI-resistant primary adenocarcinomas deduced by deconvolution analysis is shown (D).

(E) Tumorsphere formation by EpCAM^LOW CD104^HIGH LNCaP cells at the indicated times of drug treatment (n = 3 technical replicates; mean ± SD; two-tailed Student's t test; *p < 0.05).

(F) The drug sensitivity of cluster 3 was inferred by calculating the extent of correlation between cytotoxicity of each compound and cluster 3 ssGSEA score. x-axis, Z scored Pearson's correlation coefficient; y-axis, coefficient rank of compounds.

(G) Violin plots of HER family gene expression in clusters 1–6. p values by one-way ANOVA with multiple comparison by Dunnett's test are shown; ****p < 0.0001.

(H) Growth of enzalutamide-treated LNCaP cells exposed to varying concentrations of recombinant human NRG1 (rhNRG1). p values by one-way ANOVA with multiple comparison by Dunnett's test are shown; **p < 0.01; ****p < 0.0001.

(I) IB of control, drug treated, and reprogrammed LNCaP cells exposed to rhNRG1. Representative blots of n = 3 technical replicates are shown.

(J) Subpopulations of control LNCaP cells or re-LNCaP-NRG1 cells were identified by double IF with antibodies to AR and ITGB4 (see also Figure S7K). Error bars represent the mean ± SD of triplicate experiments; p values by two-tailed Student's t test; ****p < 0.0001.

(K and L) Metastatic capacity of re-LNCaP-NRG1 cells. (K) Representative BLI (left), normalized photon flux (middle), and incidence of macroscopic metastasis (right) 10 weeks after i.c. injection of re-LNCaP-NRG1 cells are shown. n = 5 per group; two independent experiments (K). NRG1 RNA FISH for NRG1 in liver metastases is shown. Counterstaining with DAPI is shown (L); scale bar represents 50 μm.

(M and N) GSEA of HER2/3 activation signatures (M) and STAT3, PI3K, mitogen-activated protein kinase (MAPK), or FGFR activation signatures in MSPC as compared with ARPC and NEPC in the SU2C-PCF dataset (N).

cancer cells to HER1/2 kinase inhibitors (Figure 4F). In addition, scRNA-seq indicated that, although quiescent, cluster 3 LNCaP cells express elevated levels of HER2 and HER3 and, to a smaller extent, EGFR (Figure 4G). We therefore reasoned that activation of HER2/3 kinase could rescue the reprogrammed LNCaP cells from growth arrest. Indeed, physiological amounts of recombinant human neuregulin-β1 (NRG1) enabled the reprogrammed LNCaP cells to proliferate in the presence of enzalutamide, but higher doses inhibited this process, presumably by interfering with HER2/3 dimerization (Yarden and Pines, 2012; Figure 4H). In contrast, EGF and fibroblast growth factor (FGF) did not rescue the proliferation of enzalutamide-tolerant cells (Figure S7G). Congruently, the reprogrammed and NRG1-rescued LNCaP cells (heretofore re-LNCaP-NRG1) exhibited elevated levels of AKT and robust activation of HER2 and the Ras-ERK and phosphatidyl inositol 3-kinase (PI3K)-mTOR pathways in response to NRG1 (Figure 4I). Control experiments indicated that these cells maintain hybrid E/M traits and do not reactivate AR signaling (Figures S7H and S7I). In addition, they contain a similarly small fraction of $AR^+ ITGB4^+$ intermediate cells as compared with control and reprogrammed LNCaP cells (Figures 4J and S7K). These results indicate that NRG1 rescues the reprogrammed LNCaP cells from growth arrest.

In contrast to parental LNCaP cells, the re-LNCaP-NRG1 cells produced macroscopic metastases in the liver and, less frequently, in the adrenal glands upon intracardiac (i.c.) injection in uncastrated mice (Figure 4K). RNA-fluorescence in situ hybridization (FISH) pointed to robust expression of NRG1 by normal hepatocytes and stromal cells in the tumor microenvironment, but not by metastatic tumor cells (Figure 4L; arrows point to stromal cells), consistent with the results of a recent study (Zhang et al., 2020). Notably, although 80% of metastatic tumor cells were AR negative or low, the remainder exhibited moderate or strong nuclear accumulation of AR (Figure S7L). Since the re-LNCaP-NRG1 cells injected in mice contained a smaller proportion of AR^+ cells, we presumed that these cells expand in castrated mice in response to adrenal androgens (Mostaghel et al., 2019). These findings indicate that HER2/3 signaling rescues the enzalutamide persister cells from growth arrest and promotes their capacity to colonize metastatic sites in response to exogenous NRG1.

Congruent with the relevance of NRG1 and HER2 signaling to human PC, GSEA of the SU2C-PCF dataset revealed that NRG1-HER2 signaling is substantially activated in MSPC, but not ARPC or NEPC (Figures 4M and 4N). In addition, reverse phase protein array (RPPA) analysis of the TCGA dataset indicated that cluster 3 gene expression strongly correlates with the phosphorylation and activation of HER1 or HER2 and components of downstream RAS-ERK, PI3K-mTOR, and JAK2-STAT3 pathways in primary PC (Figure S7J). These observations suggest that HER2/3 signaling is activated to a substantially higher level in MSPC as compared with ARPC or NEPC.

Downregulation of E2F1 and BRCA and transcriptional silencing of *TP53* marks the onset of reprogramming

To identify the oncogenic pathways involved in the transition from ARPC to MSPC, we ranked the 189 oncogenic signatures curated in the GSEA database according to their enrichment in MSPC as compared with ARPC. Intriguingly, P53_DN.V1_UP reflective of inactivation of TP53 was the top signature enriched in MSPC in the PCO-94 dataset and ranked among the top 10 signatures enriched in this subtype in the SU2C-PCF, FHCRC, and UCSF datasets (Figures 5A, S8A, and S8B). Since the *TP53* gene is not mutated at a higher rate in MSPC as compared with ARPC in these datasets (Figures 2C and 2D), we hypothesized that inhibition of AR signaling induces transcriptional silencing of wild-type *TP53* in MSPC. Congruently, AR activity (single-sample GSEA [ssGSEA] score of HALLMARK_ANDROGEN_RESPONSE) strongly correlated with the expression of *TP53* mRNA in wild-type *TP53* samples from the SU2C-PCF and FHCRC datasets (Figure S8C).

To examine whether AR blockade induces transcriptional inactivation of *TP53*, we examined the expression of *TP53* and *TP53* target genes in LNCaP cells treated with enzalutamide. Strikingly, the drug caused a rapid decline in the expression of *TP53*, *MDM2*, *CDKN1A(p21)*, *BAX*, and *BBC3 (PUMA)* and several additional canonical *TP53* targets (Figures 5B, 5C, and S8D; Fischer, 2017). Furthermore, UV irradiation induced a lower level expression of *TP53* and *NOXA* in spite of enhanced phosphorylation of TP53 at S15 in enzalutamide-treated cells as compared with naive cells, confirming that enzalutamide functionally inactivates TP53 (Figure 5D).

To dissect the mechanism leading to transcriptional inactivation of TP53, we identified TFs able to bind to the *TP53* promoter by using the ENCODE_CHIP database (Figure S8E) and selected BRCA1 and E2F1 because they were downregulated by more than 2-fold within 24 h of treatment (Figure 5E). Notably, silencing of BRCA1 or E2F1 caused a substantial repression of *TP53* mRNA and protein, and simultaneous silencing of both TFs exerted an even larger inhibitory effect, leading to near loss of protein expression, suggesting that BRCA1 and E2F1 cooperate to induce expression of TP53 (Figures 5F and 5G). ChIP-qPCR confirmed that BRCA1 and E2F1 bind directly to the *TP53* promoter in LNCaP cells (Figures S9A and S9B). Moreover, doxycycline-induced expression of short hairpin RNAs (shRNAs) targeting BRCA1 caused a significant decrease in the activation marks P-S2-Pol II and H3K4me3 and, reciprocally, an increase in the repression mark H3K27me3 associated with the *TP53* promoter, confirming that BRCA1 positively regulates *TP53* (Figure S9C). Similarly, silencing of E2F1 resulted in a decrease in the activation marks P-S2-Pol II and H3K4me3 and an increase in the repressive mark H3K27me3 at the *TP53* promoter, indicating that E2F1 also positively regulates the *TP53* promoter (Figure S9D). Silencing of Brca1 also deactivated and repressed the *Trp53* promoter and decreased p53 expression in PC cells from $Pten^{PC-/-}$ mice, and enzalutamide produced a similar effect (Figures S9E–S9G). These results suggest that BRCA1 and E2F1 jointly control the expression of *TP53* in PC cells.

Inactivation of TP53 induces hybrid E/M and stemness traits and metastatic competency

To determine whether inactivation of TP53 is sufficient to mediate reprogramming to MSPC in response to enzalutamide, we silenced TP53 in LNCaP cells. Similar to enzalutamide treatment, TP53 inactivation downregulated ZO-1, but not
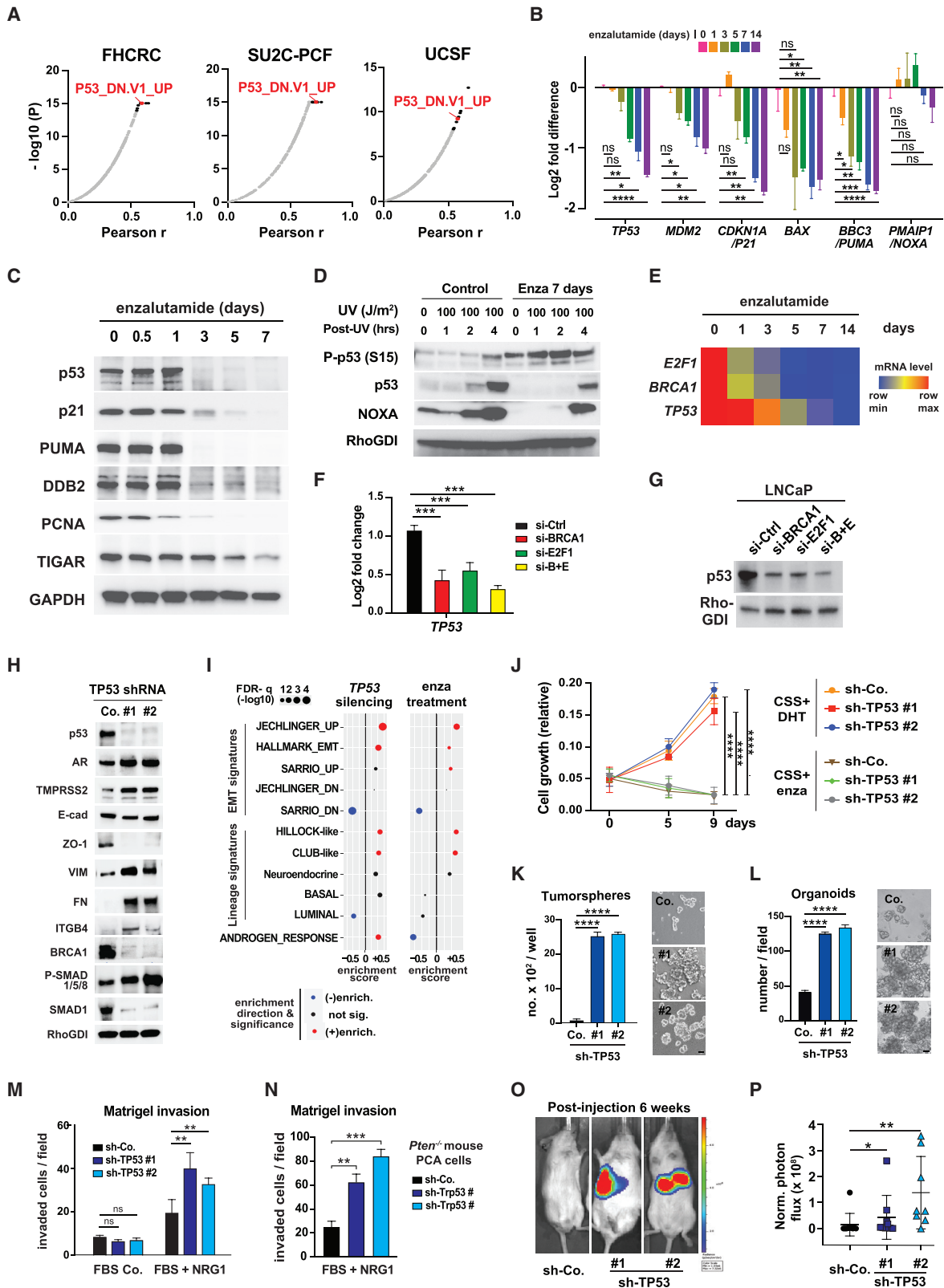
E-cadherin, and induced vimentin, fibronectin, and ITGB4. However, it did not downregulate AR or its target TMPRSS2 (Figure 5H). Furthermore, silencing of TP53 induced expression of EMT and stemness genes overlapping with those induced by enzalutamide but did not downregulate AR signaling (Figure 5I). Congruently, inactivation of TP53 did not increase the sensitivity of LNCaP cells to androgen or decrease their sensitivity to enzalutamide, suggesting that loss of TP53 does not contribute to enzalutamide resistance (Figure 5J). In addition, silencing of Trp53 increased fibronectin and N-cadherin expression but did not affect AR expression in PC cells from $Pten^{PC-/-}$ mice (Figure S9H). These results indicate that the TP53-silenced LNCaP cells are driven by AR signaling in spite of acquisition of hybrid E/M and stem-like traits.

Functional analysis indicated that the TP53-silenced cells form a larger number of tumorspheres in suspension and tumor organoids in 3D Matrigel as compared with control cells (Figures 5K and 5L). Intriguingly, although NRG1 did not increase the capacity of TP53-silenced cells to form tumorspheres or organoids (A.R. and F.G.G., unpublished data), it induced them to invade *in vitro* to a substantially larger extent as compared with control cells (Figures 5M and 5N). Similarly, silencing of Trp53 in PC cells from $Pten^{PC-/-}$ mice promoted tumorsphere formation and invasion in response to NRG1 (Figures S9I and S9J). Finally, upon i.c. injection in noncastrated non-obese diabetic (NOD) severe combined immunodeficiency (SCID) Gamma (NSG) mice, TP53-silenced LNCaP cells generated macrometastases in the liver and adrenal glands, whereas control cells did not (Figures 5O and 5P). Therefore, inactivation of TP53 induces reprogramming to a hybrid E/M and stem-like state and promotes invasion and metastasis but does not downregulate AR signaling or contribute to enzalutamide resistance.

Inhibition of BMP signaling sustains AR-independent survival and proliferation

We reasoned that the pathway or mechanism responsible for anti-androgen resistance would be activated by enzalutamide, but not loss of TP53. Therefore, we used GSEA to identify the signatures enriched in enzalutamide-treated cells as compared with TP53-silenced cells (Figure 6A; Table S6). Intriguingly, "LEE_BMP2_TARGETS_UP," which comprises genes upregulated following deletion of BMP2 (Lee et al., 2007), was the top signature found. In addition, we considered that BMP-SMAD signaling promotes the survival and differentiation of basally located stem cells in the prostatic epithelium (Mishina et al., 1995; Mou et al., 2016).

To examine whether AR blockade results in inhibition of BMP signaling and the latter contributes to dedifferentiation and enzalutamide resistance, we generated a signature reflective of BMP-R inactivation by identifying the genes modulated by the selective BMP-R1 inhibitor LDN193189 (Hao et al., 2010) in control and TP53-silenced LNCaP cells (Table S7). Notably, we found that the LDN193189_RESPONSE score is inversely correlated with the HALLMARK_ANDROGEN_RESPONSE score in the three M-CRPC datasets (Figures 6B and S10A). In addition, treatment of LNCaP cells with enzalutamide resulted in a rapid and coordinated inhibition of AR and BMP signaling, suggesting that AR signaling sustains activation of the BMP pathway (Figures 6C and 6D). Further analysis indicated that the drug downregulates the expression of BMP-R1A and B, the coreceptor *NEO*1 and the BMP-responsive SMADs, and suppresses the

Figure 5. Enzalutamide-induced transcriptional inactivation of *TP53* is mediated by BRCA1 and E2F1 and confers hybrid E/M and stemness traits

(A) Top 10 gene sets (black dots) with a ssGSEA score, which correlates positively with the MSPC proportion estimate (%) from the three M-CRPC datasets. P53_DN.V1_UP (red dot) was ranked among the top 10 signatures in all three datasets. Parental gene sets are from the C6 Oncogenic Signatures (n = 189) from the MSigDB Collection.

(B) Expression of TP53 and selected target genes in LNCaP cells treated with 10 μM enzalutamide for the indicated times. p values by two-way ANOVA and multiple comparisons test by Dunnett's method are shown. Error bars represent the mean ± SD of triplicate experiments; *p < 0.05; **p < 0.01; ***p < 0.001; ****p < 0.0001.

(C and D) IB of LNCaP cells treated with enzalutamide for the indicated times (C). Control and drug-treated LNCaP cells exposed or not to UV light (D) and subjected to IB at the indicated times are shown. Representative blots of n = 3 technical replicates are shown.

(E) Heatmap of ranked normalized *Z* scores of E2F1, BRCA1, and TP53 mRNA. Fragments per kilobase of transcript per million mapped reads (FPKM) values from RNA-seq of LNCaP cells treated with 10 μM enzalutamide for the indicated times are shown.

(F) Relative levels of TP53 mRNA in LNCaP cells transfected for 2 days with the indicated small interfering RNAs (siRNAs). Error bars represent the mean ± SD of triplicate experiments; p values by one-way ANOVA and multiple comparison by Dunnett's test are shown; ***p < 0.001.

(G) IB of p53 protein in LNCaP cells transfected for 4 days with the indicated siRNAs. Representative blots of n = 3 technical replicates are shown.

(H) Control and TP53-silenced LNCaP cells were subjected to IB with the indicated antibodies. Representative blots of n = 3 technical replicates are shown.

(I) Cluster Profiler dot plot of the enrichment of EMT (top) and cell lineage signatures (bottom) in control as compared with *TP53*-silenced (left) or enzalutamide-treated LNCaP cells (right).

(J) Cell growth of control and TP53-silenced LNCaP cells treated with CSS + DHT or CSS + enzalutamide (10 μM) at the indicated times. Error bars represent the mean ± SD of triplicate experiments; p values by one-way ANOVA and multiple comparison by Dunnett's test are shown; ****p < 0.0001.

(K and L) Quantification (left) and representative images (right) of control and *TP53*-silenced LNCaP cells subjected to tumorsphere (K) or organoid formation assay (L). Error bars represent the mean ± SD of triplicate experiments, p values are calculated by one-way ANOVA, and multiple comparison by Dunnett's test is shown; ****p < 0.0001; scale bars represent 500 μm.

(M and N) TP53-silenced LNCaP cells (M) and Trp53-silenced Pten-P8$^{(-/-)}$ cells (N) were subjected to Matrigel invasion assay with or without hrNRG1. Error bars represent the mean ± SD of triplicate experiments; p values by one-way ANOVA and multiple comparison by Dunnett's test are shown; **p < 0.01; ***p < 0.001; scale bars represent 500 μm.

(O and P) Male NGS mice were injected i.c. with 3.0 × 10^5 LNCaP cells expressing the indicated constructs and subjected 6 weeks later to bioluminescent imaging. Representative images (O) and quantification of luciferase counts (P) are shown. Error bars denote mean ± SD of five mice per group. Two independent experiments are shown; p values by one-way ANOVA and multiple comparison by Dunnett's test are shown; *p < 0.05; **p < 0.01.
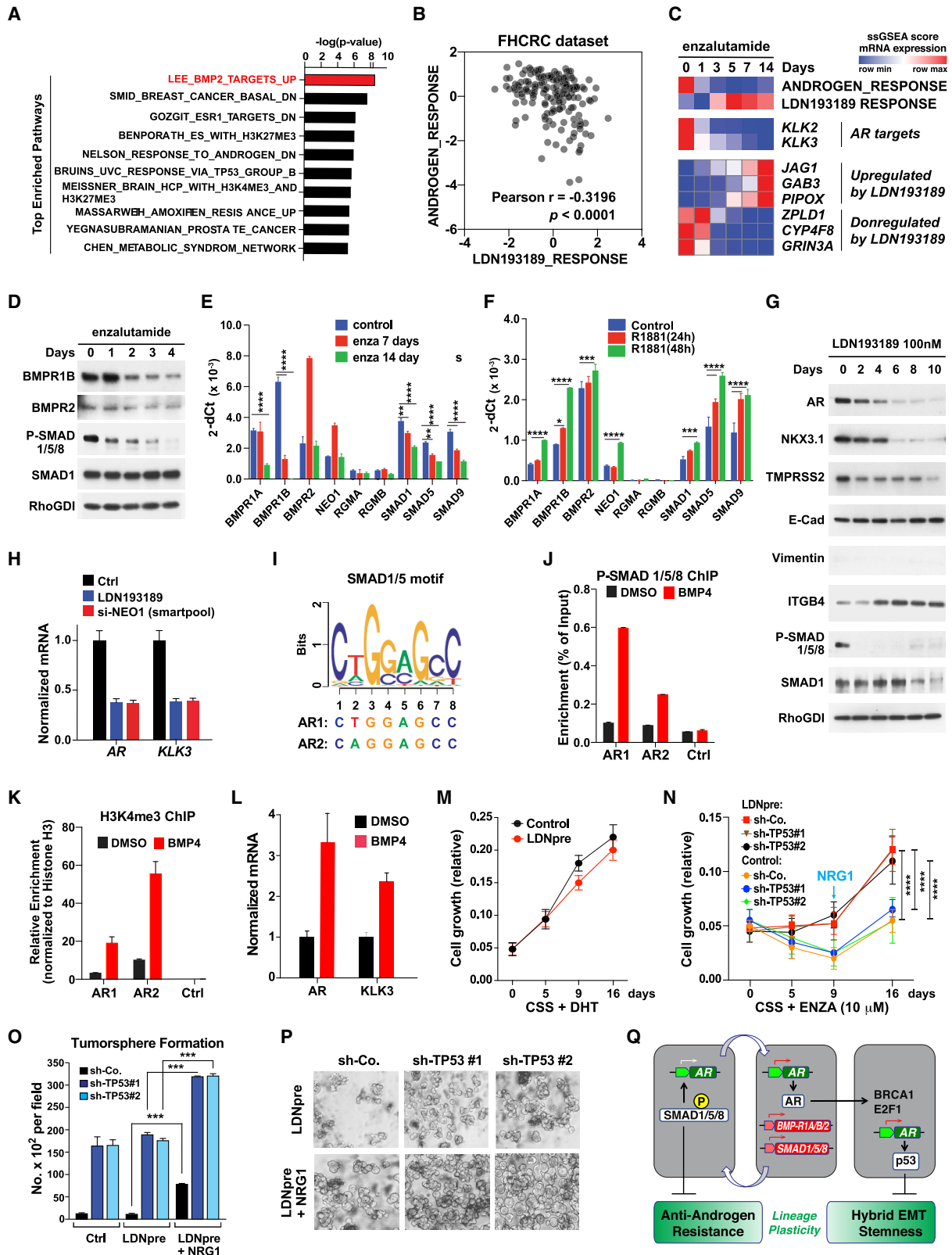
(legend on next page)

phosphorylation of BMP-responsive SMADs (Figures 6D and 6E). Stable silencing of AR induced similar changes (Gonit et al., 2011; Figure S10B; GEO: GSE22483). Conversely, the synthetic androgen R1881 increased the expression of *BMPR1A*, *BMR1B*, *NEO 1*, *SMAD1*, *SMAD5*, and *SMAD9* (Figure 6F). Consistent with its identification as the top gene expressed in ARPC, *BMPR1B* was the BMP pathway component most profoundly induced by AR signaling (Figure 2A). These results suggest that AR signaling controls, either directly or indirectly, the expression of several BMP pathway components and thereby sustains BMP signaling, explaining why blockade of the AR results in inhibition of BMP signaling.

To investigate the consequences of inhibition of BMP signaling, we treated LNCaP cells with LDN193189 over a period of 10 days. Although the compound did not inhibit cell proliferation (Figure S10C), it suppressed the expression of AR, KLK3, TMPRSS2, and the luminal lineage TF NKX3.1 and induced expression of ITGB4, but not vimentin (Figure 6G). Genetic or antibody-mediated inactivation of the essential BMP coreceptor *NEO*1 inhibited BMP signaling and downregulated the AR and the AR target gene KLK3 as efficiently as LDN193189 (Figures 6H and S10D–S10F). GSEA indicated that LDN193189 induces an enrichment of the club-like prostate luminal progenitor and the neuroendocrine signature, but not of five EMT signatures (Figures S10G and S10H). Notably, LDN193189 pretreatment did not affect tumorsphere formation by TP53-silenced LNCaP cells (Figures S10I and S10J). Therefore, inhibition of the BMP-SMAD pathway downregulates AR signaling and provokes partial dedifferentiation and lineage infidelity without inducing mesenchymal or stem-like traits.

To identify the mechanism leading to downregulation of the AR, we inspected the promoter of the AR and found two canonical SMAD1/5 binding motifs (Figure 6I). ChIP-qPCR indicated that BMP promotes binding of activated P-SMAD1/5/8 to both motifs and simultaneously enriches the activation mark H3K4me3 in the surrounding chromatin (Figures 6J and 6K). In addition, BMP promoted transcription of *AR* and *KLK3* (Figure 6L). These findings identify the AR as a target of BMP-responsive SMADs and suggest that enzalutamide downregulates the AR at least in part because it inhibits BMP signaling.

Since LDN193189 inhibited AR expression and signaling but did not inhibit proliferation, we surmised that it activates alternative pathways for survival and proliferation. We therefore asked whether inhibition of BMP signaling contributes to enzalutamide resistance. LNCaP cells pretreated with LDN193189 grew in response to androgen almost as efficiently as control cells, suggesting that they remain androgen responsive for proliferation in spite of diminished levels of AR (Figure 6M). However, they survived in the presence of enzalutamide up to 25 μM, whereas control cells did not (Figure S10K). Furthermore, the cells pretreated with LDN193189 and surviving in the presence of 10 μM enzalutamide started to proliferate in response to NRG1 and robustly expanded in the continuous presence of the drug (Figure 6N). Silencing of TP53 did not improve the performance of LDN193189-treated LNCaP cells in the presence of enzalutamide, confirming that inactivation of TP53 does not contribute to anti-androgen resistance (Figures 6N and S10K). These findings indicate that inhibition of BMP signaling promotes cell survival in the face of enzalutamide and enables subsequent expansion in response to NRG1.

We next examined the effect of inhibition of BMP signaling on stemness traits. Pretreatment with LDN193189 enhanced the capacity of control and TP53-silenced cells to form tumorspheres in the presence, but not the absence, of NRG1 (Figures 6O and 6P). The TP53-silenced cells formed a significantly higher number of spheres if they were pretreated with LDN193189 and then

Figure 6. Inactivation of BMP-SMAD signaling promotes anti-androgen resistance

(A) Top gene sets upregulated in enzalutamide-treated as compared with TP53-silenced LNCaP cells. Chemical and genetic perturbations (CGP) (3,368 gene sets) dataset from the MSigDB collection is shown. Enrichment was computed and ranked by p value.

(B) Correlation between ssGSEA score of the HALLMARK_ANDROGEN_RESPONSE and LDN193189_RESPONSE in the FHCRC dataset.

(C) Heatmap of average ssGSEA scores of the HALLMARK_ANDROGEN_RESPONSE, the LDN193189_RESPONSE, and the expression of representative AR target genes and genes suppressed or activated by BMP-SMAD signaling in LNCaP cells treated with 10 μM enzalutamide for 0–14 days. Three replicates per condition are shown.

(D) IB of BMP receptors and phosphorylation of BMP-responsive SMADs in LNCaP cells treated with enzalutamide for 0–4 days. Representative blots of n = 3 technical replicates are shown.

(E and F) qPCR of mRNAs encoding BMP-SMAD pathway components (normalized to 18S) in LNCaP cells treated with 10 μM enzalutamide for 0, 7, and 14 days (E) or 100 pM R1881 for 1 and 2 days (F). p values were determined by two-way ANOVA; multiple comparisons test by Dunnett's method is shown. Error bars represent the mean ± SD of triplicate experiments; *p < 0.05; **p < 0.01; ***p < 0.001; ****p < 0.0001.

(G) Immunoblotting of AR, AR targets, and EMT/stemness markers in LNCaP cells treated with 100 nM LDN193189 for 0–10 days. Representative blots of n = 3 technical replicates are shown.

(H) qPCR of AR and KLK3 mRNAs in serum starved LNCaP cells treated with 50 nM LDN193189 or SMART pool *NEO*1 siRNA. Error bars represent the mean ± SD of triplicate experiments.

(I–K) Schematic view of SMAD1/5 binding motifs in the AR promoter (I). Serum-starved LNCaP cells were treated for 8 h with 100 ng/mL BMP4 or DMSO and subjected to ChIP with anti-P-SMAD1/5/8 antibody (J) or H3K4me3 antibody (K). Two distal sites in the AR promoter, both containing SMAD1/5 motif (refer to I) and a negative control site in exon 2, were examined. Error bars represent the mean ± SD; n = 3 technical replicates.

(L) qPCR of AR and KLK3 mRNA in LNCaP cells treated for 1 day with 100 ng/mL BMP4 or DMSO. Error bars represent mean ± SD; n = 3 technical replicates.

(M and N) Cell growth of control and LDN193189 pretreated (8 days) LNCaP cells in response to CSS + DHT (M) and control and LDN193189 pretreated (8 days) LNCaP cells expressing the indicated control and TP53-targeted shRNAs in response to CSS + 10 μM enzalutamide (N). Error bars represent the mean ± SD; n = 3 technical replicates. p values by one-way ANOVA and multiple comparison by Dunnett's test are shown; ****p < 0.0001.

(O and P) Quantification (O) and representative images (P) of tumorspheres seeded by control and TP53-silenced LNCaP cells (day 10). Cells were treated with or without 100 nM LDN193189 and LDN193189 + rhNRG1 beginning 8 days before the assay. Error bars represent mean ± SD of triplicate experiments. p values were determined by two-way ANOVA; multiple comparisons test by Dunnett's method is shown; ***p < 0.001; scale bar represents 500 μm.

(Q) Model of the distinct transcriptional and signaling mechanisms governing acquisition of mesenchymal and stemness traits and anti-androgen resistance.
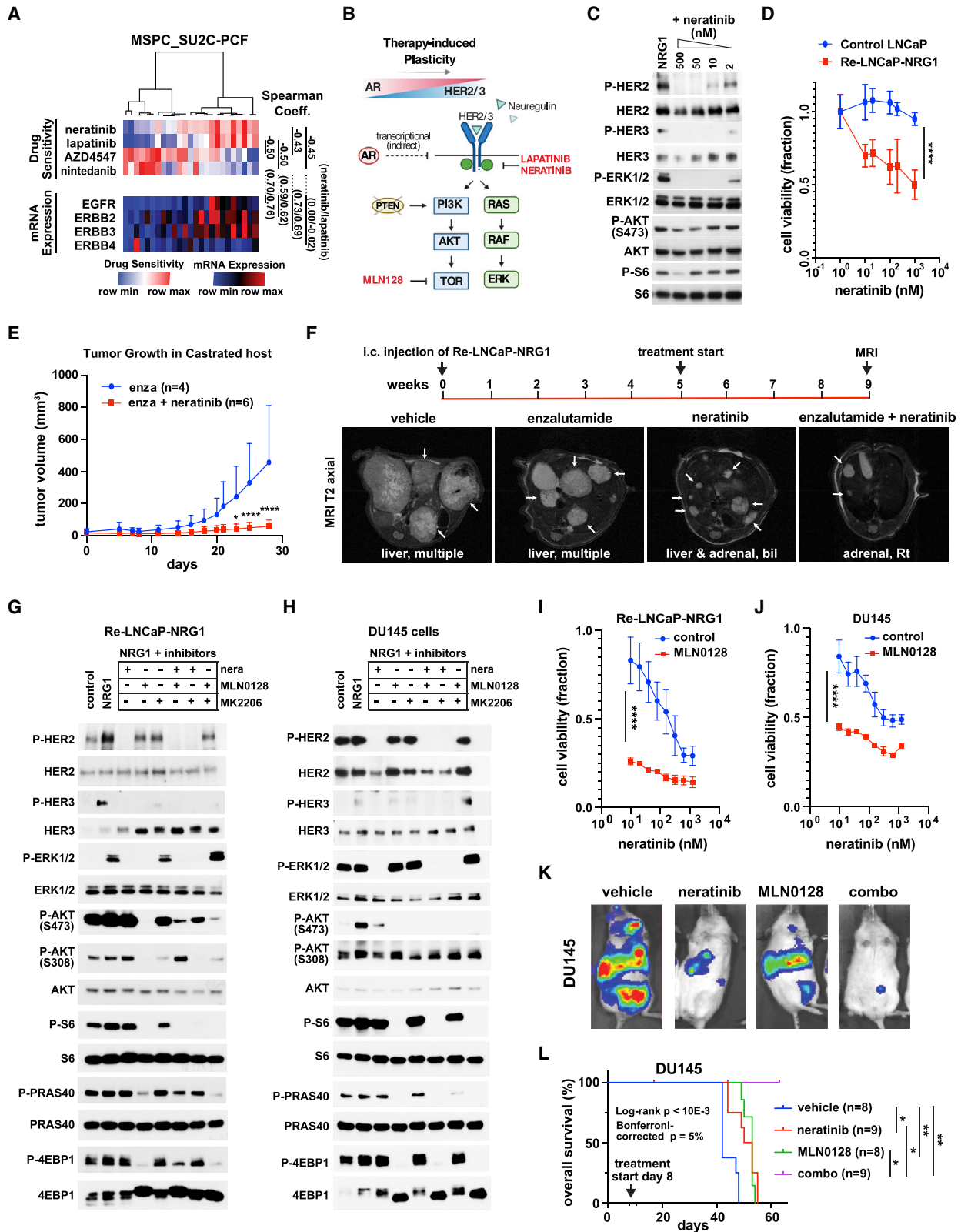
(legend on next page)

exposed to NRG1 as compared with those that had not been pre-treated, suggesting that inhibition of BMP signaling and inactivation of TP53 cooperate to sustain self-renewal in response to NRG1 (Figures 6O and 6P). Furthermore, the TP53-silenced LNCaP cells generated more organoids than control cells when pretreated with LDN193189 and cultured in androgen-depleted medium (Figure S10K). NRG1 further increased organoid formation in TP53-silenced and control cells that had been pretreated with LDN193189, suggesting that inhibition of BMP signaling and inactivation of TP53 cooperate to sustain proliferation and aberrant luminal differentiation in the absence of exogenous androgen. These results indicate that inhibition of BMP signaling promotes anti-androgen resistance and enhances NRG1-driven stemness.

Since LDN193189 inhibits AR expression and signaling but does not inhibit proliferation, we surmised that it activates alternative pathways for survival and proliferation. Intriguingly, KRAS_SIGNALING_UP and inflammatory signatures dependent on NF-κB or JAK-STAT3 signaling were among the top 10 hallmark signatures induced by LDN193189 and enzalutamide (Figure S10L). Future studies will be required to examine whether inhibition of BMP signaling promotes anti-androgen resistance through the coordinated action of NF-κB and JAK-STAT3, which previous studies have implicated in therapy resistance (Wang et al., 2020; Zhao et al., 2016). We concluded that enzalutamide paradoxically promotes the emergence of drug-resistant PC cells endowed with hybrid E/M and stem-like traits and metastatic capacity through the combined inactivation of luminal lineage-determinant BMP-SMAD signaling and tumor suppressor TP53 (Figure 6Q).

Neratinib-based combinations exert efficacy in MSPC xenograft models

MSPC is characterized by prominent activation of RAS and PI3K signaling (Figure 1C). It has been suggested that these signaling pathways are activated by FGFRs in a fraction of DNPC cases (Bluemn et al., 2017). To examine the sensitivity of MSPC to inhibition of HER2/3, we first clustered the MSPC samples from the SU2C-PCF dataset according to their inferred sensitivity to either HER or FGFR inhibitors. About half of the MSPC samples were predicted to be sensitive to the HER1/2 inhibitor lapatinib or the pan-HER inhibitor neratinib, but not to the FGFR inhibitor AZD4547 or nintedanib, and vice versa (Figure 7A, top). Indeed, correlation analysis demonstrated an inverse correlation between the predicted sensitivity of MSPC cases to the two types of inhibitors. Moreover, the anticipated sensitivity of these cases to HER inhibitors was positively correlated with elevated levels of expression of HER1–3 (Figure 7A, bottom). Examination of the FHCRC and UCSF datasets yielded similar results (Figure S11A). These observations suggest that a substantial fraction of MSPC cases may be sensitive to pan-HER inhibitors, such as neratinib.

We reasoned that therapy-induced reprogramming to MSPC provides a window of opportunity for combination therapy with enzalutamide and HER2/3 inhibitors in ARPC or mixed ARPC and MSPC and with HER2/3 inhibitors and TOR kinase inhibitors in *PTEN* mutant MSPC (Figure 7B). To test this model, we first examined the ability of neratinib to inhibit HER2/3 signaling in LNCaP cells reprogrammed with enzalutamide. Nanomolar concentrations of neratinib blocked NRG1-driven activation of HER2/3 and ERK but did not suppress activation of AKT and mTOR as anticipated from the *PTEN* mutant status of LNCaP cells (Li et al., 1997; Figure 7C). Furthermore, neratinib and lapatinib inhibited the proliferation of re-LNCaP-NRG1 cells to a substantially larger extent as compared with that of control LNCaP cells (Figures 7D and S11B). In contrast, the mTOR inhibitor MLN0128, pan-FGFR inhibitor AZD4547, or EGFR-specific inhibitor erlotinib did not produce such a differential effect: AZD4547 and erlotinib did not demonstrate discernable activity at doses lower than 1 μM in both types of cells and MLN0128 efficiently suppressed the proliferation of both types of cells at 100 nM (Figure S11B). These results indicate that the re-LNCaP cells are dependent on HER2/3 signaling.

To test the efficacy of neratinib *in vivo*, we first conducted primary tumorigenesis experiments in castrated and enzalutamide-treated mice. In spite of its inability to inhibit PI3K signaling, neratinib suppressed the capacity of re-LNCaP-NRG1 cells to produce subcutaneous tumors in these mice (Figure 7E). To examine the preclinical efficacy of neratinib in combination with enzalutamide in the metastatic setting, we inoculated re-LNCaP-NRG1 cells i.c. in castrated mice and treated them

---

Figure 7. Preclinical efficacy of combination therapies for mixed ARPC and MSPC and MSPC

(A) Heatmap of predicted drug sensitivity and expression of HER1–4 in MSPC samples from the SU2C-PCF dataset. Spearman correlation between the sensitivity scores of HER2/3 inhibitors neratinib and lapatinib and FGF inhibitors AZD4547 and nintedanib (top) and the expression of mRNA encoding HER1–4 (bottom) is shown. Spearman correlation coefficients are shown on the right.

(B) Signaling pathways activated by AR blockade and activation of HER2/3 in PTEN mutant PC cells and rationale for combination therapies.

(C) Immunoblotting of re-LNCaP-NRG1 cells treated with NRG1 in the presence of NRG1 and the indicated concentrations of neratinib. Representative blots of n = 3 technical replicates are shown.

(D) Cell viability dose-response curve of control LNCaP and re-LNCaP-NRG1 cells exposed to neratinib. Mean ± SD of triplicate experiments is shown. Two-tailed Student's t test of area under the curve (AUC) is shown; ****p < 0.0001.

(E) Subcutaneous tumor growth of re-LNCaP-NRG1 cells in castrated male NSG mice treated daily with 10 mg/kg enzalutamide and/or 40 mg/kg neratinib. Error bars represent mean ± SD. Two-tailed Student's t test of AUC is shown; *p < 0.05; ****p < 0.0001.

(F) Treatment schedule and representative MRI images of liver and adrenal gland metastases generated by re-LNCaP-NRG1 injected i.c. in castrated male NSG mice. Mice were treated daily with 10 mg/kg enzalutamide and/or 40 mg/kg neratinib for the period indicated.

(G and H) Re-LNCaP-NRG1 cells (G) and DU145 cells (H) were treated with NRG1 for 4 h with or without 100 nM MLN0128, 50 nM MLN1028, or 0.5 μM MK2206 singly or in combinations and subjected to IB with antibodies to total and activated signaling proteins. Representative blots of n = 3 technical replicates are shown.

(I and J) Cell viability dose-response curve of re-LNCaP-NRG1 cells (I) or DU145 cells (J) to 50 nM MLN0128 in combination with the indicated concentrations of neratinib. Error bars represent mean ± SD of triplicate experiments. Two-tailed Student's t test of AUC is shown; ****p < 0.0001.

(K and L) DU145 cells were injected i.c. in castrated male NSG mice. Mice were treated 8 months later with 40 mg/kg/day neratinib and/or 0.3 mg/kg/day MNL0128 for 4 weeks. Representative BLIs (K) and Kaplan-Meier survival analysis (L) are shown; *p < 0.05; **p < 0.01.

with neratinib, enzalutamide, or the combination starting at 5 weeks, when lesions are first detected by MRI. Although no treatment regimen reduced the total number of metastases, enzalutamide and, by a larger degree, the combination reduced the size of individual metastases and metastatic burden, suggesting that tumor cells dependent on AR signaling contribute to metastatic expansion *in vivo* (Figures 7F and S11C). In fact, we had observed partial restoration of AR signaling in the metastases seeded by reprogrammed LNCaP cells (Figure S7L). Importantly, enzalutamide not only induced a decrease of nuclear AR but also robustly activated HER2, explaining the higher efficacy of the enzalutamide and neratinib combination (Figure S11D). These results suggest that neratinib may increase the efficacy of enzalutamide in mixed ARPC-MSPC cases.

Given the frequent inactivation of *PTEN* in M-CRPC, we asked whether inhibition of AKT or mTOR kinase increases the efficacy of neratinib in re-LNCaP-NRG1 cells and DU145 cells, both of which are classified as *PTEN* mutant MSPC. In preliminary dosing experiments, the AKT inhibitor MKK2206 blocked AKT phosphorylation at S473 at 0.5–1 μM but caused a paradoxical overactivation of ERK in re-LNCaP-NRG1 cells, possibly due to the release of the negative feedback that AKT exerts on receptor tyrosine kinase expression and signaling (Chandarlapaty et al., 2011; Figure S11E). In contrast, the mTOR kinase inhibitors MLN0128 and AZD8055 blocked phosphorylation of S6 and AKT at Ser 473 at similarly low nanomolar concentrations without activating ERK (Figure S11F). Having identified optimal concentrations of the drugs, we examined the effect of neratinib in combination with either MKK2206 or MLN0128 in both re-LNCaP-NRG1 cells and DU145 cells. As a single agent, MLN0128 inhibited the activation of AKT and mTOR more profoundly as compared with MK2206 (Figures 7G and 7H). Moreover, MLN0128 interfered with the activation of ERK in re-LNCaP-NRG1, but not in DU145, cells. Since this effect was limited to the former cells and was followed at 1 and 2 days by overactivation of ERK, we did not investigate it further (Figure S11G). Importantly, the neratinib and MLN0128 combination was superior to other combinations in effectively and durably blocking the activation of ERK, AKT, and mTOR in both types of cells (Figures 7G, 7H, and S11G). These findings indicate that this combination profoundly inhibits mitogenic signaling through both the RAS-ERK and PI3K-mTOR pathway in *PTEN* mutant MSPC cells.

To examine the capacity of neratinib + MLN0128 to inhibit proliferation, we kept MLN0128 at 50 nM and titrated neratinib. Nanomolar doses of neratinib substantially increased the capacity of 50 nM MLN0128 to inhibit the proliferation of re-LNCaP-NRG1 and DU145 cells, but not of control LNCaP cells (Figures 7I, 7J, and S11H). In reciprocal experiments, nanomolar doses of MLN0128 increased the capacity of neratinib to inhibit the proliferation of DU145 cells (Figure S11I). Since the DU145 cells do not express the AR and possess stable MSPC traits, we used these cells to test the preclinical efficacy of neratinib in combination with MLN0128. We injected the tumor cells i.c. in castrated mice and commenced drug treatments at day 8, when tumor cells are estimated to have already seeded target organs and resisted initial attrition (Giancotti, 2013). Intriguingly, neratinib singly and in combination with MLN0128 effectively

reduced metastatic burden (Figures 7K and S11J). Interestingly, the combination reduced metastatic burden more uniformly as compared with neratinib alone and increased survival to a larger extent as compared with each single agent (Figures 7L and S11K). These results document the preclinical efficacy of neratinib, alone and in combination with MLN0128, in MSPC.

DISCUSSION

The significant genetic heterogeneity of M-CRPC hinders full understanding of the underlying biology and hence the design of effective therapies (Boutros et al., 2015; Kishan et al., 2020; Kumar et al., 2016; Quigley et al., 2018; Robinson et al., 2015). By using deconvolution analysis, we have identified three intrinsic transcriptional subtypes of M-CRPC: ARPC, MSPC, and NEPC, which partly overlap with the AR+ (ARPC), AR−/NE− (DNPC), and NE+ (NEPC) subtypes previously defined by using immunohistochemistry-based gene sets (Bluemn et al., 2017). Intriguingly, a large number of M-CRPC cases comprise subpopulations of tumor cells of distinct subtype, documenting a high degree of phenotypic heterogeneity. Mixed ARPC and MSPC and pure MSPC cases represent a substantial fraction of M-CRPCs and have become more frequent with the advent of ARSIs, suggesting that MSPC originates from ARPC as a result of therapy-induced lineage plasticity. Congruently, the MSPC component is substantially increased and the ARPC component correspondingly decreased in patients treated with ARSIs. These findings suggest that MSPC constitutes a form of adaptive resistance to ARSIs.

Infrequently, MSPC arises *de novo* at the primary site as an aggressive variant. *De novo* MSPC is enriched of *PTEN* and *TP53* mutations and exhibits elevated pathological grade and reduced time to progression, suggesting that it represents an aggressive variant (Aparicio et al., 2016). The large majority of nonresponder primary tumors in a neoadjuvant trial with ARSIs consists of MSPC, suggesting that also primary ARPC morphs into MSPC in response to AR blockade. The nonresponders to a similar trial share a transcriptional program of low AR activity and stemness reminiscent of the one described here but no distinctive oncogenic mutation (Alumkal et al., 2020), corroborating the notion that lineage plasticity supports the transformation of ARPC into MSPC.

The defining feature of MSPC is its enrichment of luminal progenitor and EMT signatures (Henry et al., 2018; Sackmann Sala et al., 2017; Smith et al., 2015; Wang et al., 2009). In addition, whereas ARPC exhibits transcriptional similarity to luminal breast cancer, MSPC resembles basal-like breast cancer (Perou et al., 2000; Sorlie et al., 2001), and MSPC and NEPC share transcriptional traits with the mesenchymal and proneural subtypes of GBM (Verhaak et al., 2010). These results indicate that the transcriptional profiles of the three subtypes of M-CRPC mirror developmental programs of the normal gland that may be shared in other organs, consistent with the hypothesis that subtype-specific programs arise from the effect of oncogenic transformation on the chromatin landscape of the cell of origin (Gupta et al., 2019).

Several mechanisms link mesenchymal and stemness programs, such as those active in MSPC, to immune evasion and

immunosuppression (Dongre and Weinberg, 2019; Naik et al., 2018). PRC1 is overactive in DNPC and promotes metastasis by inducing expression of CCL2, which enhances self-renewal and promotes recruitment of M2-like tumor-associated macrophages (TAMs) (Su et al., 2019). Accordingly, agents that target PRC1 or TAMs substantially improve the efficacy of double immune checkpoint therapy (ICT) in M-CRPC models (Lu et al., 2017; Su et al., 2019). Congruently, MSPC exhibits a higher PRC1 activity and number of M2-like TAMs and dysfunctional T cells as compared with other subtypes. Moreover, it is enriched of the metastatic melanoma anti-PD-1 nonresponders signature (Hugo et al., 2016). These observations suggest that MSPC may be particularly refractory to ICT.

Remarkably, exposure to enzalutamide and the ensuing blockade of the AR induced AR-dependent prostate adenocarcinoma cells to acquire hybrid E/M traits and become tolerant to the drug in a matter of days. Although largely quiescent, the persister tumor cells formed a large number of tumorspheres in suspension culture and exhibited tumor initiation capacity in castrated mice, in agreement with the observation that the hybrid E/M state is associated with increased stemness (Bierie et al., 2017; Pastushenko et al., 2018). ATAC-seq and ChIP-seq experiments indicated that the LNCaP cells acquire MSPC traits through reprogramming of the chromatin landscape. The enhancers and promoters driving the AR and luminal differentiation program were deactivated and those controlling EMT and stemness genes became active. Further analysis revealed that the MSPC transcriptional program is dominated by the oncogenic TFs ETS1 and NF-κB1/2, which have been previously linked to overproliferation, EMT, and immunosuppression (Massague, 2004; Taniguchi and Karin, 2018). Finally, scRNA-seq indicated that the LNCaP cells treated with enzalutamide transition from the ARPC to the MSPC subtype, which we had defined in metastatic samples, validating the model and illustrating the pathological relevance of the findings.

Notably, we found that *TP53* is broadly inactivated in MSPC as a consequence of either mutation or transcriptional silencing. Combined *TP53* and *RB1* mutations are instead prevalent in NEPC, consistent with their inferred function in transdifferentiation to the neuroendocrine fate (Ku et al., 2017; Mu et al., 2017; Zou et al., 2017). Intriguingly, enzalutamide rapidly suppressed the expression of E2F1 and BRCA1 and thereby profoundly downregulated TP53 in the *PTEN* mutant LNCaP cells. In addition, E2F1 and BRCA1 coordinately bound to the TP53 promoter and induced TP53 expression in control cells (Figure 6Q). This suggests that E2F1 not only increases TP53 stability by inducing expression of ARF (Kastenhuber and Lowe, 2017) but also induces expression of *TP53* by binding to its promoter. In contrast, BRCA1 is not a sequence-specific TF but can regulate gene expression either by promoting chromatin remodeling or by binding to sequence-specific TFs (Silver and Livingston, 2012). In addition, BRCA1 directs the expression of a subset of TP53 target genes by binding to TP53 at their promoters (Mullan et al., 2006). E2F1 and BRCA1 may induce TP53 by multiple mechanisms, potentially explaining why overactivation of TP53 is limited by strong feedback mechanisms, which inhibit E2F1 and hence alleviate overproliferation and oncogenic stress (Kastenhuber and Lowe, 2017). We postulate that E2F1-driven overproliferation

causes replication stress and thereby activates BRCA1 and that AR blockade reverses this process, enabling the accumulation of DNA damage, as observed previously (Li et al., 2017). Irrespective of mechanism, our study suggests that ARSIs induce growth arrest and apoptosis of a large fraction of PC cells but render the remainder functionally deficient of BRCA1 and TP53 activity.

Silencing of TP53 was not sufficient to suppress the expression of the AR or promote enzalutamide resistance. Accordingly, the TP53-silenced cells were able to generate metastasis, but only in non-castrated mice. Intriguingly, we found that BMP-SMAD signaling controls the expression of the AR. Conversely, AR controls the expression of BMP pathway components and hence BMP signaling in a feedforward loop, which may be necessary for aberrant differentiation (Figure 6Q). Consistent with this model, AR blockade induced inactivation of BMP signaling and decreased AR expression and signaling in LNCaP cells. However, it did not promote the expression of hybrid E/M traits, presumably because it only reduced AR signaling. Remarkably, cells pretreated with the BMP-R1 inhibitor LDN193189 resisted treatment with enzalutamide, and concurrent inactivation of TP53 enabled them to expand *in vitro* and form tumor organoids. Further studies are required to identify the mechanisms underlying the capacity of BMP-R inhibition to promote anti-androgen resistance.

Although androgen deprivation elevates the expression of HER2 in PC and HER2 signaling promotes AR stability and DNA binding (Mellinghoff et al., 2004), lapatinib or trastuzumab as monotherapy or in combination with chemotherapy, dutasteride, or ketoconazole have not demonstrated clinical activity in unselected patients (Orme and Huang, 2020). We found that the more potent pan-HER inhibitor neratinib cooperates with enzalutamide in curbing the expansion of metastases generated by enzalutamide-resistant and reprogrammed LNCaP cells. Notably, these cells contain a fraction of AR⁺ cells, which seemingly outgrow in response to adrenal androgens in untreated castrated mice. This observation suggests that the combination of neratinib and ARSI may be efficacious in cases of mixed ARPC and MSPC with elevated HER2/3 activity. The fraction of sensitive cases may be even larger, as we noted that enzalutamide induces a substantial activation of HER2. The therapeutic efficacy of enzalutamide in combination with agents targeting neuregulin signaling in ARPC models (Zhang et al., 2020) may originate from the ability of enzalutamide to induce transition from ARPC to MSPC with attendant upregulation of HER2/3 and sensitivity to its inhibition. Moreover, the combination of neratinib with the mTOR kinase inhibitor MLN0226 may be efficacious in mixed ARPC and MSPC and MSPC.

In sum, our findings identify MSPC as a sizable subtype of M-CRPC and trace its origin to therapy-induced plasticity. Rather than favoring the outgrowth of clones with certain oncogenic mutations, AR blockade is shown to directly induce reprogramming to a dedifferentiated stem-like state characterized by hybrid E/M traits and clinical aggressivity. Our results support a model in which transcriptional inactivation of TP53 induces hybrid E/M and stemness traits and inactivation of BMP signaling results in anti-androgen resistance. Finally, this study identifies HER2/3 signaling as a pathway PC cells rely on to emerge from drug-induced tolerance, an observation that deserves to be explored in biomarker-driven clinical trials.

Limitations of the study

We have documented the ability of TP53 inactivation to drive the acquisition of E/M and stemness traits in LNCaP cells and PC cells from $Pten^{PC-/-}$ mutant mice. However, the studies linking inactivation of BMP signaling to anti-androgen resistance were performed only in LNCaP cells. This limitation is only partially alleviated by the strong correlation between inactivation of AR signaling and inactivation of TP53 and BMP signaling observed in three large M-CRPC datasets. Additional studies of multiple PDX models will be needed to test whether the mechanisms described here are general or apply only to a subset of MSPCs. In fact, we noted that HER2/3 signaling and FGFR signaling are elevated in distinct subsets of MSPC. Finally, the models examined here are *PTEN* mutant, and it is therefore unclear whether the specific molecular mechanisms described here are applicable to *PTEN* wild-type cases.

STAR★METHODS

Detailed methods are provided in the online version of this paper and include the following:

- KEY RESOURCES TABLE
- RESOURCE AVAILABILITY
  - Lead contact
  - Materials availability
  - Data and code availability
- EXPERIMENTAL MODEL AND SUBJECT DETAILS
  - Cell lines
  - Generation of *Pten*-p8$^{(-/-)}$ cell line
  - Patient-derived xenograft models
  - Patient-derived organoids
  - Animals
- METHOD DETAILS
  - Stable and conditional knockdown of gene expression
  - Cell proliferation assay
  - Tumorsphere assay
  - Cell invasion assay
  - Matrigel 3D culture
  - Prostate organoid culture
  - Bioluminescence and X-Ray imaging
  - Immunohistochemistry staining
  - Immunoblotting
  - NRG1 FISH labeling experiment
  - Immunofluorescence staining
  - Datasets of patients with prostate cancer
  - Prostate cancer patient-derived xenografts, cell lines and organoids (PCO-94)
  - PCO-94 dataset clustering and determination of optimal K
  - CIBERSORT tumor deconvolution and estimation of subtype abundances
  - Bulk RNA-seq analysis
  - Single cell RNA-seq analysis
  - Single cell trajectory inference
  - Chromatin immunoprecipitation (ChIP)
  - Immune cell subset deconvolution analysis
  - Gene set enrichment analysis
  - Single sample GSEA projections and visualizations
  - Sample and library preparation for ChIP-seq and ATAC-seq
  - Analysis of ATAC-seq data
  - Analysis of ChIP-seq data
  - FACS analysis
  - Analysis of protein and mRNA expression
- QUANTIFICATION AND STATISTICAL ANALYSIS
- ADDITIONAL RESOURCES

AUTHOR CONTRIBUTIONS

F.G.G., H.H., and Y.W. conceived the study, designed and analyzed experiments, and wrote the manuscript. H.H. and Y.W. performed most of the experiments. S.G., X.W., and E.G.C. helped with enzalutamide treatment experiments. S.G., A.R., and X.W. studied TP53- and BRCA1-silenced LNCaP cells. H.H. and S.B. performed scRNA-seq experiments and J.C. pharmacological inhibition experiments. G.C. and S.G. performed experiments on BMP signaling and A.R., S.L., and Y. Jiang *in vitro* functional assays. H.C. and M.H. helped with bioinformatics analyses and N.N. with scRNA-seq. D.K., B.Z., and S.G. characterized reprogramming of the PDX model. S.N.M. performed histological analysis of the PDXs. A.R., S.L., and S.G. characterized the $Pten^{pc-/-}$ PC cells. X.W. helped with ChIP-seq; Y. Ji, A.R., and B.Z. generated reagents and animals; and N.M.N., S.N.M., and A.M.A. provided PDXs and transcriptome data. E.E. and C.J.L. provided access to the transcriptome data from the abi-enza neoadjuvant trial. Y.C. provided patient-derived organoids and critical insight.

REFERENCES

Abida, W., Cyrta, J., Heller, G., Prandi, D., Armenia, J., Coleman, I., Cieslik, M., Benelli, M., Robinson, D., Van Allen, E.M., et al. (2019). Genomic correlates of clinical outcome in advanced prostate cancer. Proc. Natl. Acad. Sci. U S A *116*, 11428–11436. https://doi.org/10.1073/pnas.1902651116.

Acevedo, V.D., Gangula, R.D., Freeman, K.W., Li, R.L., Zhang, Y.Y., Wang, F., Ayala, G.E., Peterson, L.E., Ittmann, M., and Spencer, D.M. (2007). Inducible FGFR-1 activation leads to irreversible prostate adenocarcinoma and an epithelial-to-mesenchymal transition. Cancer Cell *12*, 559–571. https://doi.org/10.1016/j.ccr.2007.11.004.

Alumkal, J.J., Sun, D.C., Lu, E., Beer, T.M., Thomas, G.V., Latour, E., Aggarwal, R., Cetnar, J., Ryan, C.J., Tabatabaei, S., et al. (2020). Transcriptional profiling identifies an androgen receptor activity-low, stemness program associated with enzalutamide resistance. P Natl. Acad. Sci. U S A *117*, 12315–12323. https://doi.org/10.1073/pnas.1922207117.

Aparicio, A.M., Shen, L., Tapia, E.L., Lu, J.F., Chen, H.C., Zhang, J., Wu, G., Wang, X., Troncoso, P., Corn, P., et al. (2016). Combined tumor suppressor defects characterize clinically defined aggressive variant prostate cancers. Clin. Cancer Res. *22*, 1520–1530. https://doi.org/10.1158/1078-0432.CCR-15-1259.

Arozarena, I., and Wellbrock, C. (2019). Phenotype plasticity as enabler of melanoma progression and therapy resistance. Nat. Rev. Cancer *19*, 377–391. https://doi.org/10.1038/s41568-019-0154-4.

Azare, J., Leslie, K., Al-Ahmadie, H., Gerald, W., Weinreb, P.H., Violette, S.M., and Bromberg, J. (2007). Constitutively activated Stat3 induces tumorigenesis and enhances cell motility of prostate epithelial cells through integrin beta 6. Mol. Cell Biol. *27*, 4444–4453. https://doi.org/10.1128/Mcb.02404-06.

Barbie, D.A., Tamayo, P., Boehm, J.S., Kim, S.Y., Moody, S.E., Dunn, I.F., Schinzel, A.C., Sandy, P., Meylan, E., Scholl, C., et al. (2009). Systematic RNA interference reveals that oncogenic KRAS-driven cancers require TBK1. Nature *462*, 108–112. https://doi.org/10.1038/nature08460.

Bass, A.J., Watanabe, H., Mermel, C.H., Yu, S.Y., Perner, S., Verhaak, R.G., Kim, S.Y., Wardwell, L., Tamayo, P., Gat-Viks, I., et al. (2009). SOX2 is an amplified lineage-survival oncogene in lung and esophageal squamous cell carcinomas. Nat. Genet. *41*, 1238–U1105. https://doi.org/10.1038/ng.465.

Beltran, H., Prandi, D., Mosquera, J.M., Benelli, M., Puca, L., Cyrta, J., Marotz, C., Giannopoulou, E., Chakravarthi, B.V., Varambally, S., et al. (2016). Divergent clonal evolution of castration-resistant neuroendocrine prostate cancer. Nat. Med. *22*, 298–305. https://doi.org/10.1038/nm.4045.

Beshiri, M.L., Tice, C.M., Tran, C., Nguyen, H.M., Sowalsky, A.G., Agarwal, S., Jansson, K.H., Yang, Q., McGowen, K.M., Yin, J., et al. (2018). A PDX/organoid biobank of advanced prostate cancers captures genomic and phenotypic heterogeneity for disease modeling and therapeutic screening. Clin. Cancer Res. *24*, 4332–4345.

Bierie, B., Pierce, S.E., Kroeger, C., Stover, D.G., Pattabiraman, D.R., Thiru, P., Liu Donaher, J., Reinhardt, F., Chaffer, C.L., Keckesova, Z., and Weinberg, R.A. (2017). Integrin-beta4 identifies cancer stem cell-enriched populations of partially mesenchymal carcinoma cells. Proc. Natl. Acad. Sci. U S A *114*, E2337–E2346. https://doi.org/10.1073/pnas.1618298114.

Blondel, V.D., Guillaume, J.-L., Lambiotte, R., and Lefebvre, E. (2008). Fast unfolding of communities in large networks. J. Stat. Mech. Theor. Exp. *2008*, 10008. https://doi.org/10.1088/1742-5468/2008/10/p10008.

Bluemn, E.G., Coleman, I.M., Lucas, J.M., Coleman, R.T., Hernandez-Lopez, S., Tharakan, R., Bianchi-Frias, D., Dumpit, R.F., Kaipainen, A., Corella, A.N., et al. (2017). Androgen receptor pathway-independent prostate cancer is sustained through FGF signaling. Cancer Cell *32*, 474. https://doi.org/10.1016/j.ccell.2017.09.003.

Boehm, J.S., Garnett, M.J., Adams, D.J., Francies, H.E., Golub, T.R., Hahn, W.C., Iorio, F., McFarland, J.M., Parts, L., and Vazquez, F. (2021). Cancer research needs a better map. Nature *589*, 514–516. https://doi.org/10.1038/d41586-021-00182-0.

Bolger, A.M., Lohse, M., and Usadel, B. (2014). Trimmomatic: a flexible trimmer for Illumina sequence data. Bioinformatics *30*, 2114–2120. https://doi.org/10.1093/bioinformatics/btu170.

Boroviak, T., Loos, R., Lombard, P., Okahara, J., Behr, R., Sasaki, E., Nichols, J., Smith, A., and Bertone, P. (2015). Lineage-specific profiling delineates the emergence and progression of naive pluripotency in mammalian embryogenesis. Dev. Cell *35*, 366–382. https://doi.org/10.1016/j.devcel.2015.10.011.

Boumahdi, S., and de Sauvage, F.J. (2020). The great escape: tumour cell plasticity in resistance to targeted therapy. Nat. Rev. Drug Discov. *19*, 39–56. https://doi.org/10.1038/s41573-019-0044-1.

Boutros, P.C., Fraser, M., Harding, N.J., de Borja, R., Trudel, D., Lalonde, E., Meng, A., Hennings-Yeomans, P.H., McPherson, A., Sabelnykova, V.Y., et al. (2015). Spatial genomic heterogeneity within localized, multifocal prostate cancer. Nat. Genet. *47*, 736. https://doi.org/10.1038/ng.3315.

Bracken, A.P., Dietrich, N., Pasini, D., Hansen, K.H., and Helin, K. (2006). Genome-wide mapping of Polycomb target genes unravels their roles in cell fate transitions. Genes Dev. *20*, 1123–1136. https://doi.org/10.1101/gad.381706.

Cai, Y.Y., Crowther, J., Pastor, T., Asbagh, L.A., Baietti, M.F., De Troyer, M., Vazquez, I., Talebi, A., Renzi, F., Dehairs, J., et al. (2016). Loss of chromosome 8p governs tumor progression and drug response by altering lipid metabolism. Cancer Cell *29*, 751–766. https://doi.org/10.1016/j.ccell.2016.04.003.

Cao, J., Spielmann, M., Qiu, X., Huang, X., Ibrahim, D.M., Hill, A.J., Zhang, F., Mundlos, S., Christiansen, L., Steemers, F.J., et al. (2019). The single-cell transcriptional landscape of mammalian organogenesis. Nature *566*, 496–502. https://doi.org/10.1038/s41586-019-0969-x.

Cerami, E., Gao, J., Dogrusoz, U., Gross, B.E., Sumer, S.O., Aksoy, B.A., Jacobsen, A., Byrne, C.J., Heuer, M.L., Larsson, E., et al. (2012). The cBio cancer genomics portal: an open platform for exploring multidimensional cancer genomics data. Cancer Discov *2*, 401–404. https://doi.org/10.1158/2159-8290.CD-12-0095.

Chandarlapaty, S., Sawai, A., Scaltriti, M., Rodrik-Outmezguine, V., Grbovic-Huezo, O., Serra, V., Majumder, P.K., Baselga, J., and Rosen, N. (2011). AKT inhibition relieves feedback suppression of receptor tyrosine kinase expression and activity. Cancer Cell *19*, 58–71. https://doi.org/10.1016/j.ccr.2010.10.031.

Charafe-Jauffret, E., Ginestier, C., Monville, F., Finetti, P., Adelaide, J., Cervera, N., Fekairi, S., Xerri, L., Jacquemier, J., Birnbaum, D., and Bertucci, F. (2006). Gene expression profiling of breast cell lines identifies potential new basal markers. Oncogene *25*, 2273–2284. https://doi.org/10.1038/sj.onc.1209254.

Chen, C.D., Welsbie, D.S., Tran, C., Baek, S.H., Chen, R., Vessella, R., Rosenfeld, M.G., and Sawyers, C.L. (2004). Molecular determinants of resistance to antiandrogen therapy. Nat Med *10*, 33–39. https://doi.org/10.1038/nm972.

Chua, C.W., Shibata, M., Lei, M., Toivanen, R., Barlow, L.J., Bergren, S.K., Badani, K.K., Mc Kiernan, J.M., Benson, M.C., Hibshoosh, H., and Shen, M.M. (2014). Single luminal epithelial progenitors can generate prostate organoids in culture. Nat. Cell Biol. *16*, 951–961. https://doi.org/10.1038/ncb3047.

Cruz-Garcia, D., Diaz-Ruiz, A., Rabanal-Ruiz, Y., Peinado, J.R., Gracia-Navarro, F., Castano, J.P., Montero-Hadjadje, M., Tonon, M.C., Vaudry, H., Anouar, Y., et al. (2012). The Golgi-associated long coiled-coil protein NECC1 participates in the control of the regulated secretory pathway in PC12 cells. Biochem. J. *443*, 387–396. https://doi.org/10.1042/BJ20110554.

de Bono, J.S., Logothetis, C.J., Molina, A., Fizazi, K., North, S., Chu, L., Chi, K.N., Jones, R.J., Goodman, O.B., Jr., Saad, F., et al. (2011). Abiraterone and increased survival in metastatic prostate cancer. N. Engl. J. Med. *364*, 1995–2005. https://doi.org/10.1056/NEJMoa1014618.

Dhimolea, E., de Matos Simoes, R., Kansara, D., Al'Khafaji, A., Bouyssou, J., Weng, X., Sharma, S., Raja, J., Awate, P., Shirasaki, R., et al. (2021). An embryonic diapause-like adaptation with suppressed myc activity enables tumor treatment persistence. Cancer Cell *39*, 240–256.e11. https://doi.org/10.1016/j.ccell.2020.12.002.

Dobin, A., Davis, C.A., Schlesinger, F., Drenkow, J., Zaleski, C., Jha, S., Batut, P., Chaisson, M., and Gingeras, T.R. (2013). STAR: ultrafast universal RNA-seq aligner. Bioinformatics *29*, 15–21. https://doi.org/10.1093/bioinformatics/bts635.

Dongre, A., and Weinberg, R.A. (2019). New insights into the mechanisms of epithelial-mesenchymal transition and implications for cancer. Nat. Rev. Mol. Cell Biol. *20*, 69–84. https://doi.org/10.1038/s41580-018-0080-4.

Efstathiou, E., Davis, J.W., Titus, M.A., Chapin, B.F., Zurita, A.J., Wen, S.J., Tapia, E.M.L.N., Hoang, A., Cornt, P.G., Wang, X.M., et al. (2016). Neoadjuvant enzalutamide (ENZA) and abiraterone acetate (AA) plus leuprolide acetate (LHRHa) versus AA plus LHRHa in localized high-risk prostate cancer (LHRPC). J. Clin. Oncol. *34*, 1336–1345. https://doi.org/10.1200/JCO.2016.34.15_suppl.5002.

Falini, B., Tiacci, E., Liso, A., Basso, K., Sabattini, E., Pacini, R., Foa, R., Pulsoni, A., Dalla Favera, R., and Pileri, S. (2004). Simple diagnostic assay for hairy cell leukaemia by immunocytochemical detection of annexin A1 (ANXA1). Lancet *363*, 1869–1870. https://doi.org/10.1016/S0140-6736(04)16356-3.

Fellmann, C., Hoffmann, T., Sridhar, V., Hopfgartner, B., Muhar, M., Roth, M., Lai, D.Y., Barbosa, I.A.M., Kwon, J.S., Guan, Y.Z., et al. (2013). An Optimized microRNA backbone for effective single-copy RNAi. Cell Rep. *5*, 1704–1713. https://doi.org/10.1016/j.celrep.2013.11.020.

Feng, J., Liu, T., Qin, B., Zhang, Y., and Liu, X.S. (2012). Identifying ChIP-seq enrichment using MACS. Nat. Protoc. *7*, 1728–1740. https://doi.org/10.1038/nprot.2012.101.

Fishilevich, S., Nudel, R., Rappaport, N., Hadar, R., Plaschkes, I., Iny Stein, T., Rosen, N., Kohn, A., Twik, M., Safran, M., et al. (2017). GeneHancer: genome-wide integration of enhancers and target genes in GeneCards. Database (Oxford) 2017. https://doi.org/10.1093/database/bax028.

Fischer, M. (2017). Census and evaluation of p53 target genes. Oncogene *36*, 3943–3956.

Foulkes, W.D., Smith, I.E., and Reis-Filho, J.S. (2010). Triple-negative breast cancer. N. Engl. J. Med. *363*, 1938–1948. https://doi.org/10.1056/NEJMra1001389.

Fraser, M., Sabelnykova, V.Y., Yamaguchi, T.N., Heisler, L.E., Livingstone, J., Huang, V., Shiah, Y.J., Yousif, F., Lin, X., Masella, A.P., et al. (2017). Genomic hallmarks of localized, non-indolent prostate cancer. Nature *541*, 359–364. https://doi.org/10.1038/nature20788.

Gao, D., Vela, I., Sboner, A., Iaquinta, P.J., Karthaus, W.R., Gopalan, A., Dowling, C., Wanjala, J.N., Undvall, E.A., Arora, V.K., et al. (2014). Organoid cultures derived from patients with advanced prostate cancer. Cell *159*, 176–187. https://doi.org/10.1016/j.cell.2014.08.016.

Gao, H., Chakraborty, G., Zhang, Z., Akalay, I., Gadiya, M., Gao, Y., Sinha, S., Hu, J., Jiang, C., Akram, M., et al. (2016). Multi-organ site metastatic reactivation mediated by non-canonical discoidin domain receptor 1 signaling. Cell *166*, 47–62. https://doi.org/10.1016/j.cell.2016.06.009.

Gardeux, V., David, F.P.A., Shajkofci, A., Schwalie, P.C., and Deplancke, B. (2017). ASAP: a web-based platform for the analysis and interactive visualization of single-cell RNA-seq data. Bioinformatics *33*, 3123–3125.

Gerhauser, C., Favero, F., Risch, T., Simon, R., Feuerbach, L., Assenov, Y., Heckmann, D., Sidiropoulos, N., Waszak, S.M., Hubschmann, D., et al. (2018). Molecular evolution of early-onset prostate cancer identifies molecular risk markers and clinical trajectories. Cancer Cell *34*, 996–1011.e8. https://doi.org/10.1016/j.ccell.2018.10.016.

Giancotti, F.G. (2013). Mechanisms governing metastatic dormancy and reactivation. Cell *155*, 750–764. https://doi.org/10.1016/j.cell.2013.10.029.

Gonit, M., Zhang, J., Salazar, M., Cui, H., Shatnawi, A., Trumbly, R., and Ratnam, M. (2011). Hormone depletion-insensitivity of prostate cancer cells is supported by the AR without binding to classical response elements. Mol. Endocrinol. *25*, 621–634.

Gotzmann, J., Fischer, A.N., Zojer, M., Mikula, M., Proell, V., Huber, H., Jechlinger, M., Waerner, T., Weith, A., Beug, H., and Mikulits, W. (2006). A crucial function of PDGF in TGF-beta-mediated cancer progression of hepatocytes. Oncogene *25*, 3170–3185. https://doi.org/10.1038/sj.onc.1209083.

Gupta, P.B., Pastushenko, I., Skibinski, A., Blanpain, C., and Kuperwasser, C. (2019). Phenotypic plasticity: driver of cancer initiation, progression, and therapy resistance. Cell Stem Cell *24*, 65–78. https://doi.org/10.1016/j.stem.2018.11.011.

Hangauer, M.J., Viswanathan, V.S., Ryan, M.J., Bole, D., Eaton, J.K., Matov, A., Galeas, J., Dhruv, H.D., Berens, M.E., Schreiber, S.L., et al. (2017). Drug-tolerant persister cancer cells are vulnerable to GPX4 inhibition. Nature *551*, 247–250. https://doi.org/10.1038/nature24297.

Hao, J., Ho, J.N., Lewis, J.A., Karim, K.A., Daniels, R.N., Gentry, P.R., Hopkins, C.R., Lindsley, C.W., and Hong, C.C. (2010). In vivo structure-activity relationship study of dorsomorphin analogues identifies selective VEGF and BMP inhibitors. ACS Chem. Biol. *5*, 245–253. https://doi.org/10.1021/cb9002865.

Heinz, S., Benner, C., Spann, N., Bertolino, E., Lin, Y.C., Laslo, P., Cheng, J.X., Murre, C., Singh, H., and Glass, C.K. (2010). Simple combinations of lineage-determining transcription factors prime cis-regulatory elements required for macrophage and B cell identities. Mol. Cell *38*, 576–589. https://doi.org/10.1016/j.molcel.2010.05.004.

Henry, G.H., Malewska, A., Joseph, D.B., Malladi, V.S., Lee, J., Torrealba, J., Mauck, R.J., Gahan, J.C., Raj, G.V., Roehrborn, C.G., et al. (2018). A cellular anatomy of the normal adult human prostate and prostatic urethra. Cell Rep. *25*, 3530–3542.e5. https://doi.org/10.1016/j.celrep.2018.11.086.

Hugo, W., Zaretsky, J.M., Sun, L., Song, C., Moreno, B.H., Hu-Lieskovan, S., Berent-Maoz, B., Pang, J., Chmielowski, B., Cherry, G., et al. (2016). Genomic and transcriptomic features of response to anti-PD-1 therapy in metastatic melanoma. Cell *165*, 35–44. https://doi.org/10.1016/j.cell.2016.02.065.

Jechlinger, M., Grunert, S., Tamir, I.H., Janda, E., Ludemann, S., Waerner, T., Seither, P., Weith, A., Beug, H., and Kraut, N. (2003). Expression profiling of epithelial plasticity in tumor progression. Oncogene *22*, 7155–7169. https://doi.org/10.1038/sj.onc.1206887.

Jiang, P., Gu, S.Q., Pan, D., Fu, J.X., Sahu, A., Hu, X.H., Li, Z.Y., Traugh, N., Bu, X., Li, B., et al. (2018). Signatures of T cell dysfunction and exclusion predict cancer immunotherapy response. Nat. Med. *24*, 1550. https://doi.org/10.1038/s41591-018-0136-1.

Jiao, J., Wang, S.Y., Qiao, R., Vivanco, I., Watson, P.A., Sawyers, C.L., and Wu, H. (2007). Murine cell lines derived from Pten null prostate cancer show the critical role of PTEN in hormone refractory prostate cancer development. Cancer Res. *67*, 6083–6091. https://doi.org/10.1158/0008-5472.Can-06-4202.

Johnson, W.E., Li, C., and Rabinovic, A. (2007). Adjusting batch effects in microarray expression data using empirical Bayes methods. Biostatistics *8*, 118–127. https://doi.org/10.1093/biostatistics/kxj037.

Justilien, V., Walsh, M.P., Ali, S.A., Thompson, E.A., Murray, N.R., and Fields, A.P. (2014). The PRKCI and SOX2 oncogenes are coamplified and cooperate to activate hedgehog signaling in lung squamous cell carcinoma. Cancer Cell *25*, 139–151. https://doi.org/10.1016/j.ccr.2014.01.008.

Kastenhuber, E.R., and Lowe, S.W. (2017). Putting p53 in context. Cell *170*, 1062–1078. https://doi.org/10.1016/j.cell.2017.08.028.

Keenan, A.B., Torre, D., Lachmann, A., Leong, A.K., Wojciechowicz, M.L., Utti, V., Jagodnik, K.M., Kropiwnicki, E., Wang, Z.C., and Ma'ayan, A. (2019). ChEA3: transcription factor enrichment analysis by orthogonal omics integration. Nucleic Acids Res. *47*, W212–W224. https://doi.org/10.1093/nar/gkz446.

Kent, W.J., Sugnet, C.W., Furey, T.S., Roskin, K.M., Pringle, T.H., Zahler, A.M., and Haussler, D. (2002). The human genome browser at UCSC. Genome Res. *12*, 996–1006. https://doi.org/10.1101/gr.229102.

Kim, D., Pertea, G., Trapnell, C., Pimentel, H., Kelley, R., and Salzberg, S.L. (2013). TopHat2: accurate alignment of transcriptomes in the presence of insertions, deletions and gene fusions. Genome Biol. *14*, R36. https://doi.org/10.1186/gb-2013-14-4-r36.

Kishan, A.U., Romero, T., Alshalalfa, M., Liu, Y., Tran, P.T., Nickols, N.G., Ye, H.H., Sajed, D., Rettig, M.B., Reiter, R.E., et al. (2020). Transcriptomic heterogeneity of Gleason grade group 5 prostate cancer. Eur. Urol. *78*, 327–332. https://doi.org/10.1016/j.eururo.2020.05.009.

Kron, K.J., Murison, A., Zhou, S., Huang, V., Yamaguchi, T.N., Shiah, Y.J., Fraser, M., van der Kwast, T., Boutros, P.C., Bristow, R.G., and Lupien, M. (2017). TMPRSS2-ERG fusion co-opts master transcription factors and activates NOTCH signaling in primary prostate cancer. Nat. Genet. *49*, 1336–1345. https://doi.org/10.1038/ng.3930.

Ku, S.Y., Rosario, S., Wang, Y., Mu, P., Seshadri, M., Goodrich, Z.W., Goodrich, M.M., Labbe, D.P., Gomez, E.C., Wang, J., et al. (2017). Rb1 and Trp53 cooperate to suppress prostate cancer lineage plasticity, metastasis, and antiandrogen resistance. Science *355*, 78–83. https://doi.org/10.1126/science.aah4199.

Kumar, A., Coleman, I., Morrissey, C., Zhang, X.T., True, L.D., Gulati, R., Etzioni, R., Bolouri, H., Montgomery, B., White, T., et al. (2016). Substantial interindividual and limited intraindividual genomic diversity among tumors from men with metastatic prostate cancer. Nat. Med. *22*, 369. https://doi.org/10.1038/nm.4053.

Kuruma, H., Matsumoto, H., Shiota, M., Bishop, J., Lamoureux, F., Thomas, C., Briere, D., Los, G., Gleave, M., Fanjul, A., and Zoubeidi, A. (2013). A novel antiandrogen, compound 30, suppresses castration-resistant and MDV3100-resistant prostate cancer growth in vitro and in vivo. Mol. Cancer Ther. *12*, 567–576. https://doi.org/10.1158/1535-7163.Mct-12-0798.

Labrecque, M.P., Coleman, I.M., Brown, L.G., True, L.D., Kollath, L., Lakely, B., Nguyen, H.M., Yang, Y.C., da Costa, R.M.G., Kaipainen, A., et al. (2019). Molecular profiling stratifies diverse phenotypes of treatment-refractory metastatic castration-resistant prostate cancer. J. Clin. Invest. *129*, 4492–4505. https://doi.org/10.1172/Jci128212.

Langmead, B., and Salzberg, S.L. (2012). Fast gapped-read alignment with Bowtie 2. Nat. Methods *9*, 357–359. https://doi.org/10.1038/nmeth.1923.

Lee, K.Y., Jeong, J.W., Wang, J.R., Ma, L.J., Martin, J.F., Tsai, S.Y., Lydon, J.P., and DeMayo, F.J. (2007). Bmp2 is critical for the murine uterine decidual response. Mol. Cell Biol. *27*, 5468–5478. https://doi.org/10.1128/Mcb.00342-07.

Lee, Y.C., Cheng, C.J., Bilen, M.A., Lu, J.F., Satcher, R.L., Yu-Lee, L.Y., Gallick, G.E., Maity, S.N., and Lin, S.H. (2011). BMP4 promotes prostate tumor growth in bone through osteogenesis. Cancer Res. *71*, 5194–5203. https://doi.org/10.1158/0008-5472.CAN-10-4374.

Li, H., Handsaker, B., Wysoker, A., Fennell, T., Ruan, J., Homer, N., Marth, G., Abecasis, G., and Durbin, R.; 1000 Genome Project Data Processing Subgroup (2009). The sequence alignment/map format and SAMtools. Bioinformatics *25*, 2078–2079. https://doi.org/10.1093/bioinformatics/btp352.

Li, J., Yen, C., Liaw, D., Podsypanina, K., Bose, S., Wang, S.I., Puc, J., Miliaresis, C., Rodgers, L., McCombie, R., et al. (1997). PTEN, a putative protein tyrosine phosphatase gene mutated in human brain, breast, and prostate cancer. Science *275*, 1943–1947. https://doi.org/10.1126/science.275.5308.1943.

Li, L.K., Karanika, S., Yang, G., Wang, J.X., Park, S., Broom, B.M., Manyam, G.C., Wu, W.H., Luo, Y., Basourakos, S., et al. (2017). Androgen receptor inhibitor-induced "BRCAness" and PARP inhibition are synthetically lethal for castration-resistant prostate cancer. Sci. Signal. *10*, eaam7479. https://doi.org/10.1126/scisignal.aam7479.

Li, Z.G., Mathew, P., Yang, J., Starbuck, M.W., Zurita, A.J., Liu, J., Sikes, C., Multani, A.S., Efstathiou, E., Lopez, A., et al. (2008). Androgen receptor-negative human prostate cancer cells induce osteogenesis in mice through FGF9-mediated mechanisms. J. Clin. Invest. *118*, 2697–2710. https://doi.org/10.1172/JCI33093.

Liberzon, A., Birger, C., Thorvaldsdottir, H., Ghandi, M., Mesirov, J.P., and Tamayo, P. (2015). The Molecular Signatures Database (MSigDB) hallmark gene set collection. Cell Syst *1*, 417–425. https://doi.org/10.1016/j.cels.2015.12.004.

Liu, Y., Mo, J.Q., Hu, Q.D., Boivin, G., Levin, L., Lu, S., Yang, D., Dong, Z.Y., and Lu, S. (2009). Targeted overexpression of Vav3 oncogene in prostatic epithelium induces nonbacterial prostatitis and prostate cancer. Cancer Res. *69*, 6396–6406.

Love, M.I., Huber, W., and Anders, S. (2014). Moderated estimation of fold change and dispersion for RNA-seq data with DESeq2. Genome Biol *15*, 550. https://doi.org/10.1186/s13059-014-0550-8.

Lu, X., Horner, J.W., Paul, E., Shang, X.Y., Troncoso, P., Deng, P.N., Jiang, S., Chang, Q., Spring, D.J., Sharma, P., et al. (2017). Effective combinatorial immunotherapy for castration-resistant prostate cancer. Nature *543*, 728. https://doi.org/10.1038/nature21676.

Martin, M. (2011). Cutadapt removes adapter sequences from high-throughput sequencing reads. EMBnet.journal *17*, 3. https://doi.org/10.14806/ej.17.1.200.

Massague, J. (2004). G1 cell-cycle control and cancer. Nature *432*, 298–306. https://doi.org/10.1038/nature03094.

McInnes, L., Healy, J., and Melville, J. (2018). UMAP: uniform manifold approximation and projection for dimension reduction. Preprint at arXiv, 1802.03426.

Mellinghoff, I.K., Vivanco, I., Kwon, A., Tran, C., Wongvipat, J., and Sawyers, C.L. (2004). HER2/neu kinase-dependent modulation of androgen receptor function through effects on DNA binding and stability. Cancer Cell *6*, 517–527. https://doi.org/10.1016/j.ccr.2004.09.031.

Mishina, Y., Suzuki, A., Ueno, N., and Behringer, R.R. (1995). Bmpr encodes a type I bone morphogenetic protein receptor that is essential for gastrulation during mouse embryogenesis. Gene Dev. *9*, 3027–3037. https://doi.org/10.1101/gad.9.24.3027.

Mootha, V.K., Lindgren, C.M., Eriksson, K.F., Subramanian, A., Sihag, S., Lehar, J., Puigserver, P., Carlsson, E., Ridderstrale, M., Laurila, E., et al. (2003). PGC-1alpha-responsive genes involved in oxidative phosphorylation are coordinately downregulated in human diabetes. Nat. Genet. *34*, 267–273. https://doi.org/10.1038/ng1180.

Mostaghel, E.A., Zhang, A.L., Hernandez, S., Marck, B.T., Zhang, X.T., Tamae, D., Biehl, H.E., Tretiakova, M., Bartlett, J., Burns, J., et al. (2019). Contribution of adrenal glands to intratumor androgens and growth of castration-resistant prostate cancer. Clin. Cancer Res. *25*, 426–439. https://doi.org/10.1158/1078-0432.Ccr-18-1431.

Mou, H., Vinarsky, V., Tata, P.R., Brazauskas, K., Choi, S.H., Crooke, A.K., Zhang, B., Solomon, G.M., Turner, B., Bihler, H., et al. (2016). Dual SMAD signaling inhibition enables long-term expansion of diverse epithelial basal cells. Cell Stem Cell *19*, 217–231. https://doi.org/10.1016/j.stem.2016.05.012.

Mu, P., Zhang, Z., Benelli, M., Karthaus, W.R., Hoover, E., Chen, C.C., Wongvipat, J., Ku, S.Y., Gao, D., Cao, Z., et al. (2017). SOX2 promotes lineage plasticity and antiandrogen resistance in TP53- and RB1-deficient prostate cancer. Science *355*, 84–88. https://doi.org/10.1126/science.aah4307.

Mullan, P.B., Quinn, J.E., and Harkin, D.P. (2006). The role of BRCA1 in transcriptional regulation and cell cycle control. Oncogene *25*, 5854–5863. https://doi.org/10.1038/sj.onc.1209872.

Naik, S., Larsen, S.B., Cowley, C.J., and Fuchs, E. (2018). Two to tango: dialog between immunity and stem cells in health and disease. Cell *175*, 908–920. https://doi.org/10.1016/j.cell.2018.08.071.

Navone, N.M., van Weerden, W.M., Vessella, R.L., Williams, E.D., Wang, Y., Isaacs, J.T., Nguyen, H.M., Culig, Z., van der Pluijm, G., Rentsch, C.A., et al. (2018). Movember GAP1 PDX project: an international collection of serially transplantable prostate cancer patient-derived xenograft (PDX) models. Prostate *78*, 1262–1282. https://doi.org/10.1002/pros.23701.

Newman, A.M., Liu, C.L., Green, M.R., Gentles, A.J., Feng, W., Xu, Y., Hoang, C.D., Diehn, M., and Alizadeh, A.A. (2015). Robust enumeration of cell subsets from tissue expression profiles. Nat. Methods *12*, 453–457. https://doi.org/10.1038/nmeth.3337.

Nguyen, H.M., Vessella, R.L., Morrissey, C., Brown, L.G., Coleman, I.M., Higano, C.S., Mostaghel, E.A., Zhang, X., True, L.D., Lam, H.M., et al. (2017). LuCaP prostate cancer patient-derived xenografts reflect the molecular heterogeneity of advanced disease an–d serve as models for evaluating cancer therapeutics. Prostate *77*, 654–671. https://doi.org/10.1002/pros.23313.

Orme, J.J., and Huang, H.J. (2020). Microenvironment-mediated resistance to anti-androgen therapy. Cancer Cell *38*, 155–157. https://doi.org/10.1016/j.ccell.2020.07.007.

Palanisamy, N., Yang, J., Shepherd, P.D.A., Li-Ning-Tapia, E.M., Labanca, E., Manyam, G.C., Ravoori, M.K., Kundra, V., Araujo, J.C., Efstathiou, E., et al. (2020). The MD Anderson prostate cancer patient-derived xenograft series (MDA PCa PDX) captures the molecular landscape of prostate cancer and facilitates marker-driven therapy development. Clin. Cancer Res. *26*, 4933–4946. https://doi.org/10.1158/1078-0432.CCR-20-0479.

Park, J.W., Lee, J.K., Sheu, K.M., Wang, L., Balanis, N.G., Nguyen, K., Smith, B.A., Cheng, C., Tsai, B.L., Cheng, D., et al. (2018). Reprogramming normal human epithelial tissues to a common, lethal neuroendocrine cancer lineage. Science *362*, 91–95. https://doi.org/10.1126/science.aat5749.

Pastushenko, I., Brisebarre, A., Sifrim, A., Fioramonti, M., Revenco, T., Boumahdi, S., Van Keymeulen, A., Brown, D., Moers, V., Lemaire, S., et al. (2018). Identification of the tumour transition states occurring during EMT. Nature *556*, 463. https://doi.org/10.1038/s41586-018-0040-3.

Pelossof, R., Fairchild, L., Huang, C.H., Widmer, C., Sreedharan, V.T., Sinha, N., Lai, D.Y., Guan, Y., Premsrirut, P.K., Tschaharganeh, D.F., et al. (2017). Prediction of potent shRNAs with a sequential classification algorithm. Nat. Biotechnol. *35*, 350–353. https://doi.org/10.1038/nbt.3807.

Perou, C.M., Sorlie, T., Eisen, M.B., van de Rijn, M., Jeffrey, S.S., Rees, C.A., Pollack, J.R., Ross, D.T., Johnsen, H., Akslen, L.A., et al. (2000). Molecular portraits of human breast tumours. Nature *406*, 747–752. https://doi.org/10.1038/35021093.

Pomerantz, M.M., Li, F.G., Takeda, D.Y., Lenci, R., Chonkar, A., Chabot, M., Cejas, P., Vazquez, F., Cook, J., Shivdasani, R.A., et al. (2015). The androgen receptor cistrome is extensively reprogrammed in human prostate tumorigenesis. Nat. Genet. *47*, 1346. https://doi.org/10.1038/ng.3419.

Pomerantz, M.M., Qiu, X.T., Zhu, Y.Y., Takeda, D.Y., Pan, W.T., Baca, S.C., Gusev, A., Korthauer, K.D., Severson, T.M., Ha, G., et al. (2020). Prostate cancer reactivates developmental epigenomic programs during metastatic progression. Nat. Genet. *52*, 790. https://doi.org/10.1038/s41588-020-0664-8.

Qian, J., Hassanein, M., Hoeksema, M.D., Harris, B.K., Zou, Y., Chen, H.D., Lu, P.C., Eisenberg, R., Wang, J., Espinosa, A., et al. (2015). The RNA binding protein FXR1 is a new driver in the 3q26-29 amplicon and predicts poor prognosis in human cancers. Proc. Natl. Acad. Sci. U S A *112*, 3469–3474. https://doi.org/10.1073/pnas.1421975112.

Qiu, X., Mao, Q., Tang, Y., Wang, L., Chawla, R., Pliner, H.A., and Trapnell, C. (2017). Reversed graph embedding resolves complex single-cell trajectories. Nat. Methods *14*, 979–982. https://doi.org/10.1038/nmeth.4402.

Quigley, D.A., Dang, H.X., Zhao, S.G., Lloyd, P., Aggarwal, R., Alumkal, J.J., Foye, A., Kothari, V., Perry, M.D., Bailey, A.M., et al. (2018). Genomic hallmarks and structural variation in metastatic prostate cancer (vol 174, pg 758, 2018). Cell *175*, 889. https://doi.org/10.1016/j.cell.2018.10.019.

Quinlan, A.R., and Hall, I.M. (2010). BEDTools: a flexible suite of utilities for comparing genomic features. Bioinformatics *26*, 841–842. https://doi.org/10.1093/bioinformatics/btq033.

Quintanal-Villalonga, A., Chan, J.M., Yu, H.A., Pe'er, D., Sawyers, C.L., Sen, T., and Rudin, C.M. (2020). Lineage plasticity in cancer: a shared pathway of therapeutic resistance. Nat. Rev. Clin. Oncol. *17*, 360–371. https://doi.org/10.1038/s41571-020-0340-z.

Rees, M.G., Seashore-Ludlow, B., Cheah, J.H., Adams, D.J., Price, E.V., Gill, S., Javaid, S., Coletti, M.E., Jones, V.L., Bodycombe, N.E., et al. (2016). Correlating chemical sensitivity and basal gene expression reveals mechanism of action. Nat. Chem. Biol. *12*, 109. https://doi.org/10.1038/Nchembio.1986.

Ritchie, M.E., Phipson, B., Wu, D., Hu, Y.F., Law, C.W., Shi, W., and Smyth, G.K. (2015). Limma powers differential expression analyses for RNA-sequencing and microarray studies. Nucleic Acids Res. *43*, e47. https://doi.org/10.1093/nar/gkv007.

Robinson, D., Van Allen, E.M., Wu, Y.M., Schultz, N., Lonigro, R.J., Mosquera, J.M., Montgomery, B., Taplin, M.E., Pritchard, C.C., Attard, G., et al. (2015). Integrative clinical genomics of advanced prostate cancer. Cell *162*, 454. https://doi.org/10.1016/j.cell.2015.06.053.

Sackmann Sala, L., Boutillon, F., Menara, G., De Goyon-Pelard, A., Leprevost, M., Codzamanian, J., Lister, N., Pencik, J., Clark, A., Cagnard, N., et al. (2017). A rare castration-resistant progenitor cell population is highly enriched in Pten-null prostate tumours. J. Pathol. *243*, 51–64. https://doi.org/10.1002/path.4924.

Sarrio, D., Rodriguez-Pinilla, S.M., Hardisson, D., Cano, A., Moreno-Bueno, G., and Palacios, J. (2008). Epithelial-mesenchymal transition in breast cancer relates to the basal-like phenotype. Cancer Res. *68*, 989–997. https://doi.org/10.1158/0008-5472.CAN-07-2017.

Sartor, O., de Bono, J., Chi, K.N., Fizazi, K., Herrmann, K., Rahbar, K., Tagawa, S.T., Nordquist, L.T., Vaishampayan, N., El-Haddad, G., et al. (2021). Lutetium-177-PSMA-617 for metastatic castration-resistant prostate cancer. N. Engl. J. Med. *385*, 1091–1103. https://doi.org/10.1056/NEJMoa2107322.

Scher, H.I., Fizazi, K., Saad, F., Taplin, M.E., Sternberg, C.N., Miller, K., de Wit, R., Mulders, P., Chi, K.N., Shore, N.D., et al. (2012). Increased survival with enzalutamide in prostate cancer after chemotherapy. N. Engl. J. Med. *367*, 1187–1197. https://doi.org/10.1056/NEJMoa1207506.

Schneider, C.A., Rasband, W.S., and Eliceiri, K.W. (2012). NIH Image to ImageJ: 25 years of image analysis. Nat Methods *9*, 671–675. https://doi.org/10.1038/nmeth.2089.

Scognamiglio, R., Cabezas-Wallscheid, N., Thier, M.C., Altamura, S., Reyes, A., Prendergast, A.M., Baumgartner, D., Carnevalli, L.S., Atzberger, A., Haas, S., et al. (2016). Myc depletion induces a pluripotent dormant state mimicking diapause. Cell *164*, 668–680. https://doi.org/10.1016/j.cell.2015.12.033.

Silver, D.P., and Livingston, D.M. (2012). Mechanisms of BRCA1 tumor suppression. Cancer Discov. *2*, 679–684. https://doi.org/10.1158/2159-8290.Cd-12-0221.

Sircar, K., Huang, H., Hu, L., Cogdell, D., Dhillon, J., Tzelepi, V., Efstathiou, E., Koumakpayi, I.H., Saad, F., Luo, D., et al. (2012). Integrative molecular profiling reveals asparagine synthetase is a target in castration-resistant prostate cancer. Am. J. Pathol. *180*, 895–903. https://doi.org/10.1016/j.ajpath.2011.11.030.

Smith, B.A., Sokolov, A., Uzunangelov, V., Baertsch, R., Newton, Y., Graim, K., Mathis, C., Cheng, D., Stuart, J.M., and Witte, O.N. (2015). A basal stem cell signature identifies aggressive prostate cancer phenotypes. Proc. Natl. Acad. Sci. U S A *112*, E6544–E6552. https://doi.org/10.1073/pnas.1518007112.

Sorlie, T., Perou, C.M., Tibshirani, R., Aas, T., Geisler, S., Johnsen, H., Hastie, T., Eisen, M.B., van de Rijn, M., Jeffrey, S.S., et al. (2001). Gene expression patterns of breast carcinomas distinguish tumor subclasses with clinical implications. Proc. Natl. Acad. Sci. U S A *98*, 10869–10874. https://doi.org/10.1073/pnas.191367098.

Stuart, T., Butler, A., Hoffman, P., Hafemeister, C., Papalexi, E., Mauck, W.M., 3rd Hao, Y., Stoeckius, M., Smibert, P., and Satija, R. (2019). Comprehensive Integration of Single-Cell Data. Cell *177*, 1888–1902 e1821. https://doi.org/10.1016/j.cell.2019.05.031.

Su, A.I., Wiltshire, T., Batalov, S., Lapp, H., Ching, K.A., Block, D., Zhang, J., Soden, R., Hayakawa, M., Kreiman, G., et al. (2004). A gene atlas of the mouse and human protein-encoding transcriptomes. Proc. Natl. Acad. Sci. U S A *101*, 6062–6067.

Su, W.J., Han, H.H., Wang, Y., Zhang, B.Y., Zhou, B., Cheng, Y.M., Rumandla, A., Gurrapu, S., Chakraborty, G., Su, J., et al. (2019). The polycomb repressor complex 1 drives double-negative prostate cancer metastasis by coordinating stemness and immune suppression. Cancer Cell *36*, 139–155.e10. https://doi.org/10.1016/j.ccell.2019.06.009.

Subramanian, A., Tamayo, P., Mootha, V.K., Mukherjee, S., Ebert, B.L., Gillette, M.A., Paulovich, A., Pomeroy, S.L., Golub, T.R., Lander, E.S., and Mesirov, J.P. (2005). Gene set enrichment analysis: a knowledge-based approach for interpreting genome-wide expression profiles. Proc Natl Acad Sci U S A *102*, 15545–15550. https://doi.org/10.1073/pnas.0506580102.

Taniguchi, K., and Karin, M. (2018). NF-kappaB, inflammation, immunity and cancer: coming of age. Nat. Rev. Immunol. *18*, 309–324. https://doi.org/10.1038/nri.2017.142.

Thompson, T.C., Southgate, J., Kitchener, G., and Land, H. (1989). Multistage carcinogenesis induced by ras and myc oncogenes in a reconstituted organ. Cell *56*, 917–930. https://doi.org/10.1016/0092-8674(89)90625-9.

Tomlins, S.A., Mehra, R., Rhodes, D.R., Cao, X., Wang, L., Dhanasekaran, S.M., Kalyana-Sundaram, S., Wei, J.T., Rubin, M.A., Pienta, K.J., et al. (2007). Integrative molecular concept modeling of prostate cancer progression. Nat. Genet. *39*, 41–51.

Tran, C., Ouk, S., Clegg, N.J., Chen, Y., Watson, P.A., Arora, V., Wongvipat, J., Smith-Jones, P.M., Yoo, D., Kwon, A., et al. (2009). Development of a second-generation antiandrogen for treatment of advanced prostate cancer. Science *324*, 787–790. https://doi.org/10.1126/science.1168175.

Trapnell, C., Cacchiarelli, D., Grimsby, J., Pokharel, P., Li, S., Morse, M., Lennon, N.J., Livak, K.J., Mikkelsen, T.S., and Rinn, J.L. (2014). The dynamics and regulators of cell fate decisions are revealed by pseudotemporal ordering of single cells. Nat. Biotechnol. *32*, 381–386. https://doi.org/10.1038/nbt.2859.

Trapnell, C., Hendrickson, D.G., Sauvageau, M., Goff, L., Rinn, J.L., and Pachter, L. (2013). Differential analysis of gene regulation at transcript resolution with RNA-seq. Nat. Biotechnol. *31*, 46–53. https://doi.org/10.1038/nbt.2450.

Tzelepi, V., Zhang, J., Lu, J.F., Kleb, B., Wu, G., Wan, X., Hoang, A., Efstathiou, E., Sircar, K., Navone, N.M., et al. (2012). Modeling a lethal prostate cancer variant with small-cell carcinoma features. Clin. Cancer Res. *18*, 666–677. https://doi.org/10.1158/1078-0432.CCR-11-1867.

Verhaak, R.G., Hoadley, K.A., Purdom, E., Wang, V., Qi, Y., Wilkerson, M.D., Miller, C.R., Ding, L., Golub, T., Mesirov, J.P., et al. (2010). Integrated genomic analysis identifies clinically relevant subtypes of glioblastoma characterized by abnormalities in PDGFRA, IDH1, EGFR, and NF1. Cancer Cell *17*, 98–110. https://doi.org/10.1016/j.ccr.2009.12.020.

Wallace, T.A., Prueitt, R.L., Yi, M., Howe, T.M., Gillespie, J.W., Yfantis, H.G., Stephens, R.M., Caporaso, N.E., Loffredo, C.A., and Ambs, S. (2008). Tumor immunobiological differences in prostate cancer between African-American and European-American men. Cancer Res. *68*, 927–936.

Wang, G., Lu, X., Dey, P., Deng, P., Wu, C.C., Jiang, S., Fang, Z., Zhao, K., Konaparthi, R., Hua, S., et al. (2016). Targeting YAP-dependent MDSC infiltration impairs tumor progression. Cancer Discov. *6*, 80–95. https://doi.org/10.1158/2159-8290.CD-15-0224.

Wang, X., Fang, Y., Sun, W., Xu, Z., Zhang, Y., Wei, X., Ding, X., and Xu, Y. (2020). Endocrinotherapy resistance of prostate and breast cancer: importance of the NFkappaB pathway (Review). Int. J. Oncol. *56*, 1064–1074. https://doi.org/10.3892/ijo.2020.4990.

Wang, X., Kruithof-de Julio, M., Economides, K.D., Walker, D., Yu, H.L., Halili, M.V., Hu, Y.P., Price, S.M., Abate-Shen, C., and Shen, M.M. (2009). A luminal epithelial stem cell that is a cell of origin for prostate cancer. Nature *461*, 495–U461. https://doi.org/10.1038/nature08361.

Watson, P.A., Arora, V.K., and Sawyers, C.L. (2015). Emerging mechanisms of resistance to androgen receptor inhibitors in prostate cancer. Nat. Rev. Cancer *15*, 701–711. https://doi.org/10.1038/nrc4016.

Xue, W., Kitzing, T., Roessler, S., Zuber, J., Krasnitz, A., Schultz, N., Revill, K., Weissmueller, S., Rappaport, A.R., Simon, J., et al. (2012). A cluster of cooperating tumor-suppressor gene candidates in chromosomal deletions. Proc. Natl. Acad. Sci. U S A *109*, 8212–8217. https://doi.org/10.1073/pnas.1206062109.

Yarden, Y., and Pines, G. (2012). The ERBB network: at last, cancer therapy meets systems biology. Nat. Rev. Cancer *12*, 553–563. https://doi.org/10.1038/nrc3309.

Yegnasubramanian, S., Haffner, M.C., Zhang, Y., Gurel, B., Cornish, T.C., Wu, Z., Irizarry, R.A., Morgan, J., Hicks, J., DeWeese, T.L., et al. (2008). DNA hypomethylation arises later in prostate cancer progression than CpG island hypermethylation and contributes to metastatic tumor heterogeneity. Cancer Res. *68*, 8954–8967.

Yoshioka, T., Otero, J., Chen, Y., Kim, Y.M., Koutcher, J.A., Satagopan, J., Reuter, V., Carver, B., de Stanchina, E., Enomoto, K., et al. (2013). beta4 Integrin signaling induces expansion of prostate tumor progenitors. J. Clin. Invest. *123*, 682–699. https://doi.org/10.1172/JCI60720.

Zhang, Z.D., Karthaus, W.R., Lee, Y.S., Gao, V.R., Wu, C., Russo, J.W., Liu, M.H., Mota, J.M., Abida, W., Linton, E., et al. (2020). Tumor microenvironment-derived NRG1 promotes antiandrogen resistance in prostate cancer. Cancer Cell *38*, 279. https://doi.org/10.1016/j.ccell.2020.06.005.

Zhao, C., Li, H., Lin, H.J., Yang, S., Lin, J., and Liang, G. (2016). Feedback activation of STAT3 as a cancer drug-resistance mechanism. Trends Pharmacol. Sci. *37*, 47–61. https://doi.org/10.1016/j.tips.2015.10.001.

Zou, M., Toivanen, R., Mitrofanova, A., Floch, N., Hayati, S., Sun, Y.P., Le Magnen, C., Chester, D., Mostaghel, E.A., Califano, A., et al. (2017). Transdifferentiation as a mechanism of treatment resistance in a mouse model of castration-resistant prostate cancer. Cancer Discov. *7*, 736–749. https://doi.org/10.1158/2159-8290.Cd-16-1174.

STAR★METHODS

KEY RESOURCES TABLE

REAGENT or RESOURCE	SOURCE	IDENTIFIER
Antibodies		
Antibodies are listed in Table S8	N/A	N/A
Biological samples		
Patient-derived organoids	From Yu Chen lab, Memorial Sloan Kettering Cancer Center (MSKCC)	N/A
Patient-derived xenografts (PDX)	From Nora M. Navone lab, UT MD Anderson Cancer Center (MDACC)	N/A
Chemicals, peptides, and recombinant proteins		
DMEM	ThermoFisher Scientific	11965-092
RPMI 1640	ThermoFisher Scientific	61870-036
Ham's F-12K	ThermoFisher Scientific	21127022
BRFF-HPC1™	AthenaES	0403
PrEGM BulletKit	Lonza	CC-3166
PrEBM Basal Medium	Lonza	CC-3165
PrEGM SingleQout Kit Suppl & Growth Factor	Lonza	CC-4177
L-glutamine	Corning	25005CI
B27 supplement	ThermoFisher Scientific	17504044
N2 supplement	ThermoFisher Scientific	17502048
Insulin-Transferrin-Selenium (ITS-G) (100X)	Life Technologies	41400045
penicillin G-streptomycin	Corning	30004CI
Accutase	STEMCELL Technologies	07920
Trypsin-EDTA (0.05%)	ThermoFisher Scientific	25300054
FBS CD STRIPPED 500mL	Gemini Bio Products	100-119
Lipofectamine RNAiMAX	Life Technologies	13778030
LDN-193189 HCl	Selleck Chemicals	S750710
Bosutinib (SKI-606)	Selleck Chemicals	S1014
Saracatinib (AZD0530)	Selleck Chemicals	S1006
AZD4547	Selleck Chemicals	S2801
Sorafenib Tosylate	Selleck Chemicals	S1040
Sapanisertib (INK 128, MLN0128, TAK-228)	Selleck Chemicals	S2811
Neratinib	MedChem Express	HY-32721
Recombinant human NRG1-B1/HRG1-B1	R&D systems	396HB050
Recombinant human EGF	R&D systems	236-EG-200
Recombinant human FGF	ThermoFisher Scientific	PHG0261
Recombinant human BMP-4	Sigma-Aldrich	SRP3016-10UG
R1881 >=98%(HPLC)	Sigma-Aldrich	R0908-10MG
Critical commercial assays		
CHIP-IT High Sensitivity Kit	ActiveMotif	53040
Cell Counting Kit-8	BIMAKE	B34304
CellTiter-Glo	Promega	G7573
BioCoat Matrigel Invasion Chamber	Corning	354480
Chromium™ Single Cell A Chip Kit, 16 rxns	10X Genomics	1000009
Chromium™ Single Cell 3′ Library & Gel Bead Kit v2, 16 rxns	10X Genomics	120237
Chromium™ i7 Multiplex Kit, 96 rxns	10X Genomics	120262

(Continued on next page)

Continued

REAGENT or RESOURCE	SOURCE	IDENTIFIER
Deposited data		
Raw and analyzed RNA-seq data	This paper	GEO: GSE162225
Raw and analyzed CHIPseq data	This paper	GEO: GSE162293
Raw and analyzed ATACseq data	This paper	GEO: GSE162227
MDA-PCa PDX cDNA microarray	Tzelepi et al., 2012	Table S10
MDACC prostate cancer dataset	Efstathiou et al., 2016	Table S11
SU2C prostate cancer dataset	Robinson et al., 2015	dbGap: phs000915.v1.p1
UCSF prostate cancer dataset	Quigley et al., 2018	dbGAP: phs001648.v1.p1
FHCRC prostate cancer dataset	Kumar et al., 2016	GEO: GSE77930
TCGA prostate cancer dataset	The Cancer Genome Atlas Research Network	http://www.cbioportal.org/study.do?cancer_study_id=prad_tcga_pub
CPC-GENE localized, non-indolent prostate cancer dataset	(Fraser et al., 2017)	GEO: GSE84043
DKFZ early-onset prostate cancer	(Gerhauser et al., 2018)	https://www.cbioportal.org/study/summary?id=prostate_dkfz_2018
MSKCC prostate cancer organoids / organoid-derived xenografts dataset	(Gao et al., 2014)	GEO: GSE60612
Broad Institute prostate cancer cell line dataset	Cancer Cell Line Encyclopedia (CCLE)	https://sites.broadinstitute.org/ccle/
LuCaP patient-derived xenograft dataset	Nguyen et al., 2017	GEO: GSE93809
LuCaP patient-derived organoid dataset	Beshiri et al., 2018	GEO: GSE113741
The Molecular Signatures Database (MSigDB)	the GSEA software, a joint project of UC San Diego and Broad Institute (Yegnasubramanian et al., 2008)	https://www.gsea-msigdb.org/gsea/msigdb/collections.jsp
Experimental models: Cell lines		
LNCaP	ATCC	CRL-1740
LNCaP-AR	From Charles Sawyers	C. D. Chen et al. Nature Medicine (2004)
VCaP	ATCC	CRL-2876
DU145	ATCC	HTB-81
PC3	ATCC	CRL-1435
NCI-H660	ATCC	CRL-5813
RM1	From Timothy Thompson	Thompson et al., 1989
Pten-p8	ATCC	CRL-3031
Experimental models: Organisms/strains		
NOD.Cg-Prkdc Il2rg/SzJ mice	The Jackson Laboratory	5557
C57BL/6J mice	The Jackson Laboratory	664
FVB/NJ mice	The Jackson Laboratory	1800
Oligonucleotides		
Oligonucleotides are listed in Table S9	N/A	N/A
Software and algorithms		
ImageJ	Schneider et al., 2012	https://imagej.nih.gov/ij/
Bowtie2	Langmead and Salzberg, 2012	http://bowtie-bio.sourceforge.net/bowtie2/index.shtml
Samtools	Li et al., 2009	http://samtools.sourceforge.net/
Homer	Heinz et al., 2010	http://homer.ucsd.edu/homer/
R	R Development Core Team, 2016	https://www.r-project.org/
GSEA 20.0.5	Subramanian, et al., 2005	https://www.gsea-msigdb.org/gsea/index.jsp
STAR 2.7.10a	Dobin et al., 2013	https://github.com/alexdobin/STAR

Continued

REAGENT or RESOURCE	SOURCE	IDENTIFIER
DESeq2	Love et al., 2014	https://bioconductor.org/packages/release/bioc/html/DESeq2.html
Cell Ranger	10X Genomics	https://support.10xgenomics.com/single-cell-gene-expression/software/overview/welcome
Seurat v3.2.0	Stuart et al., 2019	https://satijalab.org/seurat/
ENCODE	ENCODE Consortium	https://www.encodeproject.org
UCSC Genome Browser	Kent et al., 2002	https://genome.ucsc.edu
GeneHancer Regulatory Elements and Gene Interactions	Fishilevich et al., 2017	https://genome.ucsc.edu/cgi-bin/hgTrackUi?db=hg19&g=geneHancer
Code for generation of scRNAseq figures	This paper	https://doi.org/10.5281/zenodo.5904547

RESOURCE AVAILABILITY

Lead contact
Further information and requests for resources and reagents should be directed to and will be fulfilled by the Lead Contact, Dr. Filippo G. Giancotti (fg2532@cumc.columbia.edu).

Materials availability
Plasmids and cell lines generated in this study will be made available on request, but we may require a payment and/or a completed Materials Transfer Agreement if there is potential for commercial application.

Data and code availability
- Raw and analyzed ATACseq data have been deposited at Gene Expression Omnibus (GEO) dataset and are publicly available as of the date of publication. Accession numbers are listed in the key resources table.
- This paper analyzes existing, publicly available data, links to the datasets used are listed in the key resources table.
- All other data reported in this paper will be shared by the lead contact upon request.
- All original code has been deposited at GitHub and is publicly available as of the date of publication. DOIs are listed in the key resources table.
- Any additional information required to reanalyze the data reported in this paper is available from the lead contact upon request.

EXPERIMENTAL MODEL AND SUBJECT DETAILS

Cell lines
LNCaP, VCaP, DU145, PC3, NCI-H660, *Pten-p8* cells were obtained from ATCC, Cells were cultured in Dulbecco's modified eagle medium (DMEM; Gibco) or RPMI 1640 medium (Gibco) supplemented with fetal calf serum (FBS, 10%; Gibco), and penicillin-streptomycin (Corning). All cell lines were grown at 37 C, 5% CO2, 95% humidity. 293FT packaging cells were from Invitrogen and cultured according to manufacturers' instructions. MDA-PCa-2B cells were obtained from Dr. Nora Navone's laboratory and cultured in BRFF-HPC1 (AthenaES, MD) supplemented with 10% FBS and Gentamycin at 37°C in 5% CO2. RM1 cells were obtained from Dr. Timothy Thompson's laboratory and cultured in DMEM supplemented with 10% FBS and penicillin-streptomycin at 37°C in 5% CO2.

Generation of *Pten*-p8$^{(-/-)}$ cell line
The murine *Pten*-p8$^{(-/-)}$ cell line was established by infecting the previously described *Pten*-p8$^{(-/+)}$ cells (Jiao et al., 2007) with pLV-EGFP-Cre vector (Plasmid #86805). After transduction, EGFP-positive cells were selected by fluorescence-activated cell sorting.

Patient-derived xenograft models
Prostate cancer patient-derived xenograft (PDX) models were developed in the Prostate Cancer PDX Program of the Department of Genitourinary Medical Oncology, UT MD Anderson Cancer Center, as previously reported (Li et al., 2008; Palanisamy et al., 2020). Partial characterization of the indicated prostate cancer PDXs was published in the following articles: MDA-PCa-118b (Li et al., 2008)); MDA-PCa-144-4, MDA-PCa-163-A and MDA-PCa-177-B (Aparicio et al., 2016); MDA-PCa-180-30 (Tzelepi et al., 2012); MDA-PCa-149-1 (Sircar et al., 2012) and MDA-PCa-133 (Lee et al., 2011). Written informed consent was obtained from patients before sample acquisition, and all samples were processed according to a protocol approved by the Institutional Review Board of MDACC. Information including the age of each patient can be found in abovementioned references. Fresh tumor chunks of

PDXs passaged *in vivo* less than 10 times were provided from the MDA Prostate Cancer PDX Program. Upon arrival, the specimens were placed in cold, sterile alpha-MEM (Gibco; Invitrogen), and small pieces were then implanted into subcutaneous pockets of 6- to 8-week-old male NOD SCID Gamma mice (NSG mice, The Jackson Laboratory). The wounds were closed by using Reflex 7 mm Wound Clips (Roboz Surgical Instrument Co.) or 3M™ Vetbond™ Tissue Adhesive. Mice were monitored weekly for tumor growth. Once the initial implanted tumors grew and reached the indicated size in mice, tumors were collected and extracts were prepared by using T-PER tissue protein extraction reagent (Thermo Fisher Scientific, Waltham, MA, USA) supplemented with a protease and phosphatase inhibitors cocktail (Roche). Frozen tumor tissues were ground with mortar and pestle, incubated with the extraction buffer (2 mL of buffer per 0.1 g of tissue) on ice for 30 min, sonicated 3 times for 10 sec on ice, centrifuged at 12,000 rpm for 5 min at 4°C, and the supernatant was collected and used for Western blot analysis. Tissue sections (4 μm) from formalin-fixed, paraffin-embedded (FFPE) PDX tumor tissue blocks were analyzed by immunohistochemical staining of AR (1:50, Dako), VIM (1:200, Hi pH, Dako) and ITGB4 (1:50, Cell Signaling) by using an Autostainer Plus (Dako North America, Inc. Carpinteria, CA).

Patient-derived organoids
Prostate cancer patient-derived organoid cultures were generated as described earlier (Gao et al., 2014). Informed consent was obtained from patients and tissue collection for research was approved by the IRB of MSKCC. Clinical information, including the age of each patient, can be found in above mentioned reference.

Animals
For all the animal experiments in the present study, the study protocols were approved by the Institutional Animal Care and Use Committee (IACUC) of UT MD Anderson Cancer Center. Male BALB/c nude mice, male NOD SCID gamma mice, male C57BL/6J mice, and male FVB/NJ mice (aged 4–6 weeks) were obtained from The Jackson Laboratory. For primary tumor growth assays, cells were resuspended in 100 μL PBS with Matrigel in 1:1 ratio and subcutaneously injected into both rear flanks. The volume of the s.c. xenograft was calculated as $V = L \times W2/2$, where L and W stand for tumor length and width, respectively. For experimental metastasis assays, cells were resuspended in 100 μL PBS and injected into the left ventricle with a 26G tuberculin syringe. For drug treatment, drug solutions were delivered either intraperitonially or by oral gavage using a 20G reuseable feeding needle (Roboz Surgical Co.). Metastatic burden was detected through noninvasive bioluminescence imaging of experimental animals using an IVIS Spectrum and Biospec 7T MRI instruments at the Small Animal Imaging Facility (SAIF). To investigate the effect of drug treatment, compounds were delivered daily through p.o. Bioluminescence signals were measured using the ROI tool in Living Image software (Xenogen).

METHOD DETAILS

Stable and conditional knockdown of gene expression
shRNAs were designed using the SplashRNA algorithm (Pelossof et al., 2017). A previously described optimized lentiviral miR-E expression backbone system was used for constitutive - SREP (red, puromycin) and inducible - LT3RENIR (red, Neomycin) – expression (Fellmann et al., 2013).

Cell proliferation assay
Cells (5×10^3 for LNCaP and PCa-2B, 2×10^3 for all other cells) were seeded in a 96-well plate for 24 hours. After 24 hours, cells were cultured in DMEM or RPMI without phenol red containing 2% (vol/vol) FBS in the presence of the indicated concentrations of compound(s). Viable cell numbers were measured by formazan formation using a Cell Counting Kit 8 (Dojindo). Apoptotic cells were detected by a standard TUNEL assay using an *in-situ* Cell Detection kit (Roche).

Tumorsphere assay
Single cells suspensions of tumor cells (1,000 cells/mL) were plated on ultra-low attachment plates and cultured in serum-free PrEGM (Lonza) supplemented with 1:50 B27, 20 ng/mL basic fibroblast growth factor (bFGF) and 40 ng/mL epidermal growth factor (EGF) for 10 days. Tumorspheres were visualized under phase contrast microscope, photographed, and counted. For serial passage, tumorspheres were collected using 70-μm cell strainers and dissociated with Accutase (Stem Cell Technologies) for 30 min at 37°C to obtain single cell suspensions.

Cell invasion assay
Cell invasion was assayed using Matrigel coated BioCoat Cell Culture Inserts (24-well plates, Corning). After Matrigel was rehydrated at room temperature, 2×10^5 cells suspended in 0.5 mL RPMI medium were plated into each insert. 0.5 mL medium with 15% FBS or CSS were added to the bottom of each well. Noninvading cells were removed after 48 hours culture. The cells on the lower surface of the membrane were stained with crystal violet.

Matrigel 3D culture
Dissociated cells were incubated in PrEGM medium (Lonza) supplemented with 1:50 B27, 20 ng/mL basic fibroblast growth factor (bFGF) and 40 ng/mL epidermal growth factor (EGF, Corning). Matrigel beds were created in 6 well plates by putting 4 separate drops

of Matrigel per well (50 μL Matrigel per drop). Plates were placed in a 37°C CO$_2$ incubator for 30 min to allow the Matrigel to solidify. For each sample, 100 μL of cell suspension was mixed with 100 μL cold Matrigel, and pipetted on top of the Matrigel bed (50 μL each). The plates were then incubated at 37°C for another 30 min. Warm PrEGM (2.5 mL) was then added to each well. The cells were cultured and monitored for 10–14 days with 50% change of medium every 3 days. For immunostaining, the cells were cultured in 8 well chamber slides. Cells were fixed with 4% paraformaldehyde for 20 minutes and subjected to a standard immunostaining protocol.

Prostate organoid culture
Mouse and human prostate cancer cell organoids were generated by using the embedding method as described earlier (Chua et al., 2014). Prostate cancer cells were resuspended in prostate organoid culture medium, consisting of: hepatocyte medium supplemented with 10 ng mL^{-1} EGF, 10 μM Y-27632 (STEMCELL Technologies), 1 × Glutamax (Gibco), 5% Matrigel (Corning) and 5% charcoal-stripped FBS, which had been heat-inactivated at 55°C for 1 h. After resuspension in prostate organoid medium, the resulting cell suspension containing 500–3,000 dissociated cells was mixed with 60 μL of Matrigel, and the mixture was pipetted around the rim of wells in a 24-well plate. The mixture was allowed to solidify for 30 min at 37°C, before addition of 400 μL organoid culture medium to each well. The culture medium was changed every other day, and organoids were counted after 8–10 days. The efficiency of organoid formation was calculated by averaging the number of organoids visible using a 10× objective. For statistical analyses, percentages of efficiency were coverted using the arcsine transformation and subjected to unpaired two-tailed Student's t-test.

Bioluminescence and X-Ray imaging
For bioluminescent imaging, mice were anesthetized and injected with 1.5 mg of D-luciferin intraperitoneally at the indicated times. Animals were imaged in an IVIS 100 chamber within 5 min after D-luciferin injection, and data were recorded using Living Image software (Xenogen). Photon fluxes were calculated by using the ROI tool in the Living Image software. Bone metastases were confirmed by X-Ray imaging using IVIS Lumina XR equipped with X-ray and Optical Overlay.

Immunohistochemistry staining
Immunohistochemical and immunofluorescent staining of paraffin-embedded sections was performed by using a Discovery XT processor (Ventana Medical Systems). Tissue sections were deparaffinized with EZPrep buffer (Ventana Medical Systems) and subjected to antigen retrieval with CC1 buffer (Ventana Medical Systems). Sections were blocked for 30 minutes with Background Buster solution (Innovex) and for 8 minutes with avidin-biotin blocking (Ventana Medical Systems). Sections were incubated with anti-AR (Abcam, ab133273 1 μg/mL); ITGB4 (Cell Signaling, cat# 14803, 0.5 μg/mL); vimentin (Cell Signaling, cat# 5741, 0.5 μg/mL); and synaptophysin (Abcam, ab32127, 1 μg/mL) antibodies for 5 hours followed by biotinylated horse anti-rabbit antibodies (Vector Labs, cat# PK6101) at 1:200 dilution (for AR, ITGB4, Vimentin) or HRP-conjugated goat anti-rabbit (PI-1000) antibodies at 1:250 dilution (for synaptophysin) for 60 minutes. Detection was performed with DAB detection kit (Ventana Medical Systems) according to manufacturer instruction. Slides were counterstained with hematoxylin and mounted using Permount (Fisher Scientific).

Immunoblotting
For immunoblotting, cells were washed twice with PBS and lysed in RIPA buffer (50 mM Tris-HCl pH 7.4, 150 mM NaCl, 1 mM EDTA, 1% Triton X-100, 1% sodium deoxycholate, and 0.1% SDS) supplemented with protease and phosphatase inhibitors (Protease/Phosphatase Inhibitor Cocktail (100X), Cell Signaling #5872). Total protein concentrations were determined by using the Pierce^{TM} BCA Protein Assay Kit (Thermo Scientific^{TM}, 23225). Protein concentrations were diluted to 1 μg/uL with Sample Buffer 4X and boiled for 5 min before gel loading.

NRG1 FISH labeling experiment
NRG1 RNA FISH was carried out according to the manufacturer's instructions (Stellaris® RNA FISH Protocol for Frozen Tissue; Biosearch Technologies, Inc., CA). A mouse NRG1 probe was labeled with CAL Fluor® Red 610 Dye and used at 5 nM. Sequences of custom probe sets are listed in key resources table. All hybridizations were performed overnight in the dark at 37°C in a humidifying chamber.

Immunofluorescence staining
Cell were plated on Falcon^{TM} Chambered Cell Culture Slides (Corning Inc) and cultured (specific conditionss and duration indicated in legends). Cells were fixed, washed, stained with antibodies (primary and secondary) and viewed on a confocal microscope

Datasets of patients with prostate cancer
Gene expression and amplification data from the patients with prostate cancer samples were acquired from the cBioportal database. Additionally, the UCSF dataset of patient with metastatic prostate cancer was kindly provided by the authors (Quigley et al., 2018). Z-score 2.0 was used as cut-off value to determine mRNA up/downregulation in a given sample. For the UCSF dataset, copy number alterations were called by using the log2 ratio bounds used in the original paper: - chr1-chr22 Gain/shallow loss/deep loss: 3/1.65/0.6- chrX, chrY Gain/loss: 1.4, 0.6. Morpheus was used for clustering and heatmap generation (https://software.broadinstitute.org/morpheus).

Prostate cancer patient-derived xenografts, cell lines and organoids (PCO-94)
Dataset generation and processing

Five gene expression datasets from castration-resistant prostate cancer patient-derived xenografts, cell lines and organoids were merged into a single data table by using HUGO gene symbols as reference. MDA PCa PDX: microarray data of MDA PCa PDX, including tumors of the same origin but grown in castrated or uncastrated hosts (133-4_cas1,2; 180-30_cas1,2) (Tzelepi et al., 2012); MSKCC PCa organoid/ODX (organoid-derived xenograft): mRNA expression (RNA Seq FPKM) data available for 10 of 12 PCa organoids (Gao et al., 2014). CCLE PCa Cell lines gene expression (RNA Seq RPKM) data (Release date: 14-Feb-2018. Broad Institute). LuCaP M-CRPC PDXs custom Agilent 44 k whole genome expression microarray (includes early/late and castration-resistant passages. GEO: GSE93809. Nguyen et al., 2017). LuCaP PDX-derived organoids (RNA Seq TPM) data (includes two repeats. GEO: GSE113741. Beshiri et al., 2018). Microarray data were transformed to non-logarithmic scale. ASAP v1 "Automated Single Cell Analysis Pipeline" (http://asap-old.epfl.ch) was utilized for following data processing.

1. Log2 conversion and batch correction using "ComBat" method (Johnson et al., 2007).
2. Plotting by classical MultiDimensional Scaling (MDS) or t-SNE.
3. Cluster Identification (see details in "PCO-94 dataset clustering").
4. Retrieval of Differentially Expressed Genes (DEGs) between clusters by using the Limma method (Ritchie et al., 2015).
5. Geneset enrichment analysis of the DEGs.

PCO-94 dataset clustering and determination of optimal K

In preliminary experiments, we used three independent clustering methods (PAM "Partitioning Around Medoids", K-Means, and Hierarchical clustering), three data sources (normalized data, MDS values and t-SNE values after dimension-reduction) and n of cluster as either two or three (suggested by silhouette analysis) for a total of 18 combinations. The largest cluster containing 50 samples (later determined as ARPC) showed 17 of 18 concordance rate across clustering combinations. The smallest cluster containing 13 samples (later determined as NEPC) showed 18 of 18 concordance across clustering combinations. Among the remaining 31 samples, 21 samples showed more than 6 of 9 concordance rate (later determined as MSPC) when n of cluster was three, and the remaining 10 samples showed inconsistent results across the combinations (later determined as mixed). Overall, about 80% of the samples were consistently clustered together in the test. In this manuscript, we used PAM as the final representative clustering method, and the MDS values as data source for clustering. To confirm the optimal n of cluster (K), we performed Consensus clustering (clustering.algorithm = SOM; cluster.by = columns; distance.measure = Euclidean; resample = subsample; merge.type = average; descent.iterations = 2,000; normalize.type = row-wise; normalization.iterations = 0), and calculated PAC (proportion of ambiguous clustering). Final optimal K was determined as three by the lowest PAC.

CIBERSORT tumor deconvolution and estimation of subtype abundances

To compute intratumoral heterogeneity, we used "CIBERSORT" deconvolution (Newman et al., 2015). We followed the "Custom Signature Genes File" tutorial - mixture file: full PCO-94 dataset after batch correction (gene n: 14,968); reference sample file: reduced PCO-94 dataset (gene n: 2,424); phenotype class file: annotation of clusters determined by PAM clustering of the full PCO-94 dataset. Specifically, the gene signature was defined by the average expression values of 2.4K differentially expressed genes from the PCO-94 clustering results. RNA-seq read-normalized gene expression values (RSEM, RPKM, and FPKM for TCGA, CPC-GENE and DKFZ, and SU2C-PCF and UCSF datasets, respectively) or microarray data (FHCRC dataset) with Entrez gene ID and HUGO gene symbol annotations were loaded as a "mixture" file. Purity was defined by the estimated abundances of each cluster type in a sample. Samples were designated as "mixed" if the largest component was <75% (cell lines, organoids, PDXs) or <60% (human tissues).

Bulk RNA-seq analysis

Total RNA was extracted from samples using TRIzol (Invitrogen, USA) and 1 μg was sent to BGI for quality testing and library construction. Libraries were sequenced on a BGISEQ-500. RNA-seq reads were aligned to the human reference genome (hg19) using Tophat (v2.1.1; https://ccb.jhu.edu/software/tophat/index.shtml) (Kim et al., 2013). Gene models of Refgene were downloaded from the Illumina's iGenomes project (https://support.illumina.com/sequencing/sequencing_software/igenome.html). FPKM (Fragments Per Kilobase of transcript per Million mapped reads) values were generated using cufflinks (v2.2.1; http://cole-trapnell-lab.github.io/cufflinks/) (Trapnell et al., 2013). Differential expression analysis was performed by using the cuffdiff function in cufflinks, considering genes with log2 fold change >4 or < −2 and false discovery rate (FDR) < 0.05 as significantly differentially expressed.

Single cell RNA-seq analysis

For single cell RNA sequencing, we used the Chromium Single Cell 3′ Library and Gel Bead Kit v2 (10X Genomics Inc) according to the manufacturer's protocol. Briefly, single cell suspensions of LNCaP cells were counted and loaded on individual lanes of a Single Cell A Chip with appropriate reagents. The chip was ran in the Chromium™ Single Cell Controller to generate single cell gel bead-in-emulsions (GEMs) for sample and cell barcoding. Libraries were generated using the 10x Genomics' protocol, pooled and sequenced by Illumina in Hiseq 4000 sequencer. Five samples (Day 0, Day 1, Day 3, Day 5, Day 7) were aligned with human genome GRCh38 using

STAR version 2.5.1b (Dobin et al., 2013) and further aggregated using Cell Ranger v2.0.2 for analysis, resulting 6,072 cells of 205,881 mean reads per cell (post-normalization) and 6,164 median genes per cell.

For clustering of the aggregated data, we used the graph-based clustering algorithm implemented in the Cell Ranger pipeline, which consists of building a sparse nearest-neighbor graph (where cells are linked if they are among the k nearest Euclidean neighbors of one another), followed by Louvain Modularity Optimization (LMO) (Blondel et al., 2008). The value of k is set to scale logarithmically with the number of cells. Additional cluster-merging approaches included performing hierarchical clustering on the cluster-medoids in PCA space and merging pairs of sibling clusters if there are no genes differentially expressed between them (with B-H adjusted p value below 0.05). The hierarchical clustering and merging is repeated until there are no more cluster pairs to merge. From the resulting 8 clusters, two of them showed significantly lower UMIs than the rest and were enriched by mitochontrial genes or ribosomal genes. They were excluded from further analysis in this manuscript.

Single cell trajectory inference
The reconstruction of single cell trajectory was done with Monocle 3 (Cao et al., 2019; Qiu et al., 2017; Trapnell et al., 2014). First the 10X Genomics Cell Ranger output was loaded into Monocle 3 using the load_cellranger_data function, and the data were pre-processed using the PCA method. Here we chose 100 principal components (PCs; num_dim = 100) to ensure that most of the variation in gene expression across all the cells was captured. The dimensionality of the data was reduced with the UMAP algorithm (McInnes et al., 2018) and mutually similar cells were grouped into clusters using a technique called Louvain community detection. Each cell is assigned not only to a cluster but also to a partition. Next, we fitted a principal graph within each partition using the learn_graph() function. Cells were ordered according to their progress along the learned trajectory. In our time series experiments, we chose cells in the UMAP space from early time point (here Control0) as "roots" of the trajectory. We mainly focused on the trajectory within the large partition.

Chromatin immunoprecipitation (ChIP)
Cells (1×10^6) were crosslinked by using 2 mM DSG for 45 min and 1% formaldehyde for 15 min, both at room temperature (RT). To stop crosslinking, glycine was added to the final concentration of 0.125 M and samples were incubated for 5 min at RT. Cells were collected from the dishes by scraping and washed 3 times with PBS. Pellets were resuspended and lysed in 0.5 mL of SDS lysis buffer (1% SDS, 10 mM EDTA, 50 mM Tris-HCl, pH 8.0 supplemented with PIC/PMSF/Sodium butyrate mix) and then incubated on ice for 10 min. The crosslinked cellular lysates were sonicated with a Diagnode sonicator. After sonication, samples were aliquoted in 1.7 mL tubes and centrifuged at max speed in an Eppendorf microfuge for 10 min at 4°C. Supernatants were transferred to new 1.7 mL tubes. To prepare chromatin immunoprecipitation samples, 0.1 mL of sonicated samples were added to 0.9 mL of dilution buffer (50 mM Tris-HCl, pH8.0, 0.167 M NaCl, 1.1% Triton X-100, 0.11% sodium deoxycholate supplemented with PIC/PMSF/Sodium butyrate mix), and then mixed with antibody bearing Dynabeads. The samples were gently mixed on a rocker O/N at 4°C and then placed on a magnetic stand and inverted several times. Beads were washed 5 times with 0.8 mL of cold buffer for 5 min, 1 time with RIPA-150, 1 time with RIPA-500, 1 time with RIPA-LiCl, and 2 times with 1xTE Buffer, pH 8.0. They were then resuspended in 200 μL freshly made Direct Elution Buffer (10 mM Tris-HCl pH 8.0, 0.3 M NaCl, 5 mM EDTA, 0.5% SDS) and incubated O/N at 65°C with 1 μL of RNase A to reverse the crosslinking. Samples were transferred to a new low-bind tube and incubated for 1–2 hrs at 55°C with 3 μL of Proteinase K. The reverse-crosslinked ChIP DNA samples were purified by using phase lock tubes and EtOH precipitation and resuspende in 25 μL of Qiagen elution buffer. DNA was finally amplified by using real-time PCR (ABI Power SYBR Green PCR mix).

Immune cell subset deconvolution analysis
Intratumoral immune cell subsets from the SU2C, FHCRC and UCSF M-CRPC datasets were analyzed by using CIBERSORT bulk transcriptome deconvolution analysis (Newman et al., 2015). We used the LM22 signature, which consist of 547 genes that accurately distinguish 22 mature human hematopoietic populations and activation states, including seven T cell types, naive and memory B cells, plasma cells, NK cells, and myeloid subsets.

Gene set enrichment analysis
We used the java GSEA v3.0 program (Yegnasubramanian et al., 2008). Gene set enrichment analyses (GSEA) were performed according to the instructions. Gene sets of Hallmark Collection, Canonical Pathway (including KEGG Pathway, Biocarta Pathway, Reactome Pathway and PID Pathway), and GO Biological Process were used. All gene sets are from the Molecular Signatures Database (MSigDB) version 7.1.

Single sample GSEA projections and visualizations
We carried out ssGSEA (Barbie et al., 2009) using the GenePattern module ssGSEA Projection (v9) (www.genepattern.org). We used Prism (v8) for data visualization and related statistical analysis. Genesets used for the analysis are from the Molecular Signature Database, including their hallmark genesets (Liberzon et al., 2015).

Sample and library preparation for ChIP-seq and ATAC-seq
ChIP-seq samples were prepared as described for ChIP. Libraries were prepared according to the standard Illumina protocol. Libraries were sequenced at the Sequencing and Microarray Facility of MDACC. For ATAC-seq, 5×10^5 LNCaP cells were prepared

and collected. Cells were then washed once with cold 1xPBS and spinned down at 500 g for 5 min at 4°C. Cells were kept on ice and subsequently resuspended in 25 μL of 2xTD buffer (Illumina Nextera kit), 2.5 μL Transposase enzyme (Illumina Nextera kit, 15,028,252) and 22.5 μL Nuclease-free water in a total of 50 μL reaction for 1 h at 37°C. The DNA was then purified using the Qiangen MinElute PCR purification kit (28,004) to a final volume of 1 μL. ATAC-seq Libraries were prepared following the Buenrostro protocol (http://www.ncbi.nlm.gov/pmc/articles/PMC4374986/) and ATAC-seq libraries were sequenced as 50 base paired-end reads on the DNBseq platform at the BGI Americas.

Analysis of ATAC-seq data

We utilized cutadapt (v1.18) (Martin, 2011) to remove the adaptor sequences or the reads shorter than 35 bp from the raw reads and then aligned the trimmed reads to the human reference genome (hg19) using default parameters in Bowtie2 (v2.4.1) (Langmead and Salzberg, 2012). The aligned reads were subsequently filtered for quality and uniquely mappable reads were retained for further analysis using Samtools (v1.10) (Li et al., 2009). Relaxed peaks were called using MACS2 (v2.1.2) (Feng et al., 2012) with a p value of 1×10^{-2}. Consensus peaks were calculated by extracting the overlap of peaks from the samples. Genome-wide read coverage was calculated by BEDTools (Quinlan and Hall, 2010). In order to calculate the ATAC-seq read density at the promoters and the enhancers, normalized read densities (RPKM, Reads Per Kilobase per Million mapped reads) were calculated across the promoter regions and the enhancer regions, respectively. The promoters used in this study were defined as 1 kb upstream and 1 kb downstream of the transcription start site based on the UCSC gene annotation. The annotation of the enhancers was from the FANTOM5 and the GenHancer. The annotation of the indicated transcription factors binding motif was from HOMER (Heinz et al., 2010). Significantly over-represented functional categories were identified by using the function "Investigate Gene Sets" from GSEA (http://software.broadinstitute.org/gsea/msigdb/annotate.jsp) (Mootha et al., 2003).

Analysis of ChIP-seq data

Sequencing reads from H3K4me3 and H3K27me3 ChIP-seq were trimmed by using trimmomatic (v0.39) (Bolger et al., 2014). The trimmed reads were then aligned to the human genome (hg19) using Bowtie2. PRC duplication reads were removed by Samtools. Peaks calling and reads density were calculated by using the same methods used for ATAC-seq. The promoters used in this study were defined as 5 kb upstream and 5 kb downstream of the transcription start site based on the UCSC gene annotation. To visualize ChIP-seq signal at individual genomic regions, we used the UCSC Genome Browser (https://genome.ucsc.edu/) (Kent et al., 2002).

FACS analysis

Cells were detached with Accutase and washed in blocking solution (HBSS supplemented with 10% FBS). Cell suspensions were incubated with the indicated antibodies for 45 minutes at 4°C and analyzed by FACS. At the endpoint of the *in vivo* experiment, blood and bone marrow cells were collected from each mouse and treated with Red Blood Cell lysis buffer for 5 minutes. Cells were then washed once with RPMI supplemented with 2% FBS, stained with indicated antibodies for 45 minutes and analyzed by FACS.

Analysis of protein and mRNA expression

For immunoblotting, cells were washed with PBS and lysed in RIPA buffer (50 mM Tris-HCl pH 7.4, 150 mM NaCl, 1 mM EDTA, 1% Triton X-100, 1% sodium deoxycholate, and 0.1% SDS) supplemented with protease inhibitors (Calbiochem) and phosphatase inhibitors (PhosSTOP, Roche Life Science). Protein concentrations were measured by using the DC Protein Assay. Total RNA was extracted using the RNeasy Mini kit coupled with RNase-free DNase set (Qiagen) and reverse transcribed with SuperScript^{TM} IV VILO^{TM} Master Mix with ezDNase^{TM} Enzyme (Invitrogen). cDNA corresponding to approximately 10 ng of starting RNA was used for one reaction. qPCR was performed with Taqman Gene Expression Assay (Applied Biosystems). All quantifications were normalized to endogenous GAPDH.

QUANTIFICATION AND STATISTICAL ANALYSIS

All of the statistical details including the statistical tests used, exact number of animals, definition of center, and dispersion and precision measures for the experiments can be found in the figures, figure legends or in the results. Statistical analyses were performed by using R and GraphPad Prism 8 software, with a minimum of three biologically independent samples for significance. For subcutaneous injection experiments, each subcutaneous tumor was considered an independent sample. For intracardiac injection experiments and survival analyses, each mouse was counted as a biologically independent sample. Results are reported as mean ± SD or mean ± SEM. Comparisons between two groups were performed by using an unpaired two-sided Student's t-test (p < 0.05 was considered significant). Comparison of multiple conditions was performed by using the one- or two-way ANOVA test. For correlation analysis, we used the Spearman and Pearson coefficients. All experiments were reproduced at least three times, unless otherwise indicated.

ADDITIONAL RESOURCES

E.E. and C.J.L. provided access to the transcriptome data of prostate cancer tissues derived from the abiraterone-enzalutamide neo-adjuvant clinical trial "NCT01946165".